Universidad Nacional Autónoma de México

Posgrado en Astrofísica

Instituto de Astronomía

ANÁLISIS ESPECTROSCÓPICO DE HH202. IMPLICACIONES SOBRE LA DESTRUCCIÓN DE POLVO E INHOMOGENEIDADES TÉRMICAS EN LA NEBULOSA DE ORIÓN

T E S I S

QUE PARA OPTAR POR EL GRADO DE:

MAESTRO EN CIENCIAS (ASTROFÍSICA)

PRESENTA:

JOSÉ NORBERTO ESPÍRITU CONTRERAS

DIRECTOR DE TESIS:

DR. ANTONIO PEIMBERT TORRES

INSTITUTO DE ASTRONOMÍA

MÉXICO, CIUDAD DE MÉXICO, ENERO 2017

Agradecimientos

A mis padres María Eréndira y José, por el amor que me han brindado a lo largo de mi vida, por enseñarme a luchar por mis sueños y a no rendirme nunca.

A mi hermana Zaira, por enseñarme el valor del trabajo duro y por ser mi ejemplo a seguir.

A todos mis amigos, aquellos que fueron, son y serán. Porque de cada uno de ustedes me he llevado una gran enseñanza. Porque me conocieron en mis mejores y peores momentos y decidieron permanecer a mi lado. Ustedes saben quienes son. Ustedes han sido mi familia lejos de casa, mis mejores maestros, mis mejores compañeros y mis mejores alumnos. Gracias por ayudarme a crecer día con día.

A mi director de tesis, el Dr. Antonio Peimbert Torres, por transmitirme sus conocimientos de astronomía, por su infinita paciencia, por las profundas discusiones que tuvimos y por todo su apoyo.

A mis sinodales, los Doctores Christophe Morisset, Gloria Delgado Inglada, Michael Richer, Jorge García Rojas y Anabel Arrieta; por las profundas discusiones que tuvimos, por soportar mis errores de juventud, y por sus enseñanzas que mejoraron enormemente la calidad de esta tesis.

A Miriam Peña, Edmundo Moreno, y Manuel Peimbert, por orientarme en mis primeros pasos como científico.

A Bárbara Pichardo, por permitirme colaborar con el Instituto de Astronomía desde la licenciatura, por su gran apoyo y por presentarme a Antonio.

A Instituto de Astronomía de la UNAM, por otorgarme espacio y recursos para desarrollar mis estudios de maestría y la realización de esta tesis.

A mis alumnos, porque de ustedes he aprendido cosas que no se encuentran en los libros.

A los organizadores de la escuela de verano NEBULATOM 2: C. Morisset, G. Stasińska, y C. Mendoza, porque lo que aprendí en esas dos semanas en Zihuatanejo fue fundamental para llevar a cabo este trabajo.

Agradezco al Consejo Nacional de Ciencia y Tecnología (CONACyT) de México, que a través del programa 000205 me otorgó una beca durante dos años. Asimismo agradezco al proyecto PAPIIT IN 109716 que me permitió concluir la tesis.

Contents

Resumen

Una región H II es una zona de gas ionizado que producida por una estrella, o cúmulo de estrellas, que emite fotones ultravioleta. El análisis espectroscópico de las regiones H II ha sido fundamental para establecer las bases de la astrofísica contemporánea. A partir del estudio de las nebulosas de emisión ha sido posible conocer los mecanismos físicos que rigen la formación estelar, la evolución química de la galaxia, e inclusive restringir modelos cosmológicos.

La Nebulosa de Orión es la región H II más brillante del cielo nocturno y la más estudiada en la historia de la astronomía. Sus características la han convertido en el objeto de referencia para entender los fenómenos físicos y químicos presentes en regiones H II. En ella, el gas es fotoionizado principalmente por la emisión de fotones ultravioleta emitidos por el cúmulo de estrellas conocido como el Trapecio. La emisión del gas revela la presencia de elementos como helio, oxígeno, nitrógeno, hierro, azufre, entre otros.

Orión muestra la presencia de un número considerable de estructuras en su interior, como discos protoplanetarios, y flujos de gas de alta velocidad en la forma de vientos y objetos Herbig-Haro (HH). Uno de los objetos HH más prominentes descubiertos hasta la fecha es HH 202. Este objeto es de particular interés al encontrarse dentro de una región fotoionizada, donde el calentamiento del gas está dominado por la radiación estelar y no por la energía mecánica del choque. Al encontrarse en una región privilegiada, es posible además analizar su estructura con alta resolución angular.

HH 202 es central para el tema de esta tesis pues juega un papel importante en el estudio de dos mecanismos de suma relevancia para el entendimiento de las regiones H II. El papel del polvo interestelar en regiones H II ha sido un tema de estudio que aú n presenta considerables interrogantes, sobre todo en lo concerniente a su composición química y a

los procesos que propician su destrucción. Se ha establecido que los choques interestelares dominan la destrucción del polvo, sin embargo, es difícil cuantificar la fracción de polvo que sobrevive a ellos y no se ha establecido una correlación entre la velocidad del frente de onda de choque y el grado de destrucción.

Otra discusión activa en regiones H II concierne a la estructura de temperatura de las mismas. La temperatura electrónica en este tipo de objetos está determinada por el balance entre el calentamiento debido a los fotones provenientes de la estrella central y el enfriamiento producido debido a la emisión de líneas de excitación colisional de iones pesados como O^{2+} y N^{+}. Conocer esta temperatura electrónica nos permite estimar la abundancia de los iones observados. Si en una primera aproximación se supone que la temperatura es constante a lo largo de la línea de visión; podemos obtener la abundancia de un ión utilizando la temperatura obtenida directamente de los diagnósticos de iones como [O III], [N II], y [O II]; sin embargo, al comparar las abundancias iónicas determinadas con líneas de recombinación y con líneas de excitación colisional se encuentra una discrepancia sistemática en una gran cantidad de regiones H II. A esta diferencia se le conoce como el Factor de Discrepancia de Abundancias (ADF, por sus siglas en inglés).

Diversos trabajos han mostrado que en una región H II existen inhomogeneidades de temperatura no despreciables, que pueden ser modeladas por un parámetro conocido como t^2 (Peimbert 1967, Peimbert & Costero, 1969), mismas que, al ser tomadas en cuenta, modifican el valor estimado para la abundancia iónica cuando se consideran temperaturas homogéneas, reduciendo e incluso eliminando el ADF en muchos objetos. La naturaleza física detrás de dichas inhomogeneidades es aún desconocida; no obstante se ha sugerido que los choques interestelares y las zonas de alta densidad, como los discos protoplanetarios pueden contribuir sustancialmente a generarlas. Es en este sentido que HH 202 nos otorga una oportunidad única para estudiar el comportamiento y la variación espacial de las condiciones físicas del gas y las abundancias iónicas.

En esta tesis presento un estudio de HH 202 realizado con el Very Large Telescope de 8 m de diámetro ubicado en Cerro Paranal, Chile, utilizando el espectrógrafo de rendija larga conocido como FORS 1. La ventaja de utilizar esta configuración es que permite llevar a cabo un estudio espacial de los parámetros físicos y químicos que caracterizan a Orión, comparando la onda de choque con el gas circundante.

A partir de la emisión de Hα se identificó el centro de la onda de choque, mismo que coincide casi perfectamente con el máximo de emisión de las líneas de [Fe II] y [Fe III]. Estas líneas llegan a ser hasta diez veces más intensas en el centro del choque, fenómeno que solo puede ser explicado por la incorporación de hierro (Fe) a la fase gaseosa gracias a la destrucción de los granos de polvo interestelar.

Se presenta un análisis espacial de la abundancia de oxígeno calculada con CELs y RLs, encontrando que la dicrepancia entre ambas es mayor en el centro del choque, donde se vuelven irreconciliables.

Tras realizar el análisis espacial, combiné espectros del centro del choque y de las zonas donde el gas se encuentra estático con el fin de incrementar la señal a ruido para realizar un segundo análisis, del cual obtuve cuatro ventanas. A partir de los espectros combinados determiné la temperatura y densidad electrónicas del objeto y de la Nebulosa de Orión, obteniendo resultados consistentes con estudios previos.

Determiné la abundancia de helio (He), oxígeno (O), nitrógeno (N), argón (Ar), cloro (Cl), neón (Ne), azufre (S), hierro (Fe) y níquel (Ni). En todos los casos se presentan dos determinaciones: suponiendo una temperatura constante ($t^2 = 0.00$), e introduciendo inhomogeneidades térmicas ($t^2 \neq 0.00$). Un resultado interesante de estos cálculos es que el valor de t^2 es considerablemente mayor en el centro del choque que en las zonas donde el gas no está perturbado; asimismo, al introducir dicho valor resulta posible reconciliar las determinaciones de abundancias de CELs y RLs.

Por último, calculé el porcentaje de destrucción de los granos de polvo interestelar debido a la onda de choque de HH 202, siendo este del 57 %. Estimé la cantidad de oxígeno depositada en el polvo interestelar utilizando tres métodos diferentes: comparando el relación entre Fe/O y O/H para el Sol y la Nebulosa de Orión; contrastando la abundancia estelar con la de la fase gaseosa; y asumiendo la abundancia de elementos refractarios en el polvo. Promediando mis resultados con los de la literatura se obtuvo un valor para la depleción de oxígeno de 0.126 ± 0.024 dex.

Chapter 1

Introduction

1.1 H II regions

If a young star is hot enough, as in the case of O or B stars, its ultraviolet photons can ionize the surrounding interstellar medium, forming an H II region.

H II regions get their name from the hot gas that surrounds the star, composed mainly of ionized hydrogen. However, helium and other heavy elements are also present, as evidenced by emission spectra. H II regions present a large variety of shapes and sizes due to the irregular distribution of stars, gas and dust present in them. In these objects, star formation has actively taken place, and they are capable of producing thousands of stars in a few million years. After completing their evolution, massive stars explode as supernovae, which, along with stellar winds, blow away the gas from the H II region, leaving behind a cluster of stars that may be bound by gravity. O and B type stars evolve rapidly and seldom leave their parent cloud; in average, massive stars do not remain in a stable state for longer than five or six million years, before changing its spectral type.

H II regions are found in the spiral arms of galaxies along the galaxtic plane, where they can be resolved from observations in Hα, which is an indicator of ionized hydrogen. Notwithstanding, they are studied also in the ultraviolet and infrared wavelengths, since the radiation of massive stars and interstellar dust contributes to their emission as well. In particular, infrared observations allow us to resolve deeply embedded structures such as

protoplanetary disks, Herbig-Haro objects, and newly formed stars.

Typical densities in H II regions range from 10^2 to 10^6 cm^{-3}, though only those with densities in the range of 10^2 – 10^4 cm^{-3} can be observed in the optical range. Temperatures in H II regions are in the range 5000 – 15 000 K. These physical conditions combine to produce particular spectra representative of the physical processes taking place inside the nebula, many of which cannot be reproduced on Earth due to the extremely low densities found in the interstellar medium. Typical spectra of H II regions are always dominated by hydrogen and helium recombination lines and collisionally excited lines of heavy elements.

A star cannot ionize an infinite amount of gas and, effectively most H II regions are a few parsecs in size. The volume of gas the central star(s) may ionize is limited by the volume at which the rate of recombinations is equal to the rate of ionizing photons produced by the star.

In the photoionization process, those photons whose energy is higher than the ionization potential of an ion are absorbed, releasing electrons. The excess energy of every absorbed photon is then translated into kinetic energy of the free electron. Free electrons and photons determine the conditions of the gas in H II regions; particle interactions are dominated by electron-electron and ion-electron collisions, which redistribute the energy producing a state of thermal equilibrium. As a consequence, in H II regions we seek to measure the *electron temperature* and *electron density*. Temperature in a point of a nebula is fixed by the equilibrium between heating due to photoionization and cooling by emission of radiation; in the latter, heavy elements play a dominant role.

The intensity of an emission line is a function of electron density, temperature, and the abundance of the parent ion. If the first two are known, one can estimate the chemical composition of the gas. The study of the chemical composition of H II regions is an active field of work in contemporary astronomy. It has permitted us to acknowledge the existence of abundance gradients in spiral galaxies, as it has been found that, for most spirals, heavy elements increase in abundance towards the center of the galaxy (Simpson et al., 1995; Vilchez & Esteban, 1996). This has shed light into the evolutionary history of the chemical composition of galaxies which is linked to the star formation history. H II regions are also vital in the determination of primordial helium abundance –that is, the helium that was created at the beginning of the universe–; these estimations have been paramount for constraining

cosmological models (Peimbert et al., 2016).

1.2 Interstellar dust

Besides gas, the interstellar medium has an interstellar dust component whose effects cannot be ignored at all. The most immediate of them is known as *interstellar extinction*. This extinction of radiation, which affects mainly the visible and ultraviolet region of the spectrum is due to scattering and absorption by dust particles, the size of which is comparable to the wavelength of the absorbed radiation, ranging from 0.001 to $1\mu m$.

Interstellar extinction has been calculated for different lines of sight in the galaxy for numerous stars, of identical spectral type. For this effect stars are observed in pairs, comparing obscured stars against standard stars, which are nearly unaffected by dust. Extinction is also selective, that is, it depends on wavelength, having a larger impact on shorter wavelengths, blocking blue light in a higher proportion, an effect known as consequently as *interstellar reddening*.

The chemical composition of interstellar dust grains is an active field of study in contemporary astronomy. Direct spectroscopic observations of interstellar dust do not provide a complete picture of its composition since often it is difficult to distinguish spectral features of heavy elements from the continuum radiation. Alternatively, grain composition is inferred from the fact that certain elements appear to be underabundant in the interstellar medium, a phenomenon known as *depletion*. The available evidence indicates that the overall abundances in the ISM are close to the values in the solar photosphere; direct observations show that elements like carbon (C), magnesium (Mg), silicon (Si) and iron (Fe) effectively are underabundant in the gas phase; particularly 90% of iron is incorporated in dust grains in diffuse interstellar clouds, including H II regions (Rodríguez & Rubin, 2005; Peimbert & Peimbert, 2010). Models and reddening curves have shown that interstellar dust is heterogeneous in its composition. From this, it has been inferred that the bulk of interstellar dust is composed by a mixture of the following materials (Draine, 2011):

- Silicates, e.g., pyroxene composition $Mg_xFe_{1-x}SiO_3$, or olivine composition $Mg_2xFe_{2-2x}SiO_4$ $(0 \leq x \leq 1)$

- Oxides of silicon, magnesium and iron (e.g., SiO_2, MgO, Fe_3O_4)
- Carbon solids (graphite, amorphous carbon, and diamond)
- Hydrocarbons
- Carbides (e.g. SiC)
- Metallic Fe

Other elements, like Titanium (Ti) and Chromium (Cr) are also present in interstellar grains, but, because of their low abundances, contribute only a minor fraction of the grain mass. Water ice exists in dark molecular clouds as evidenced from an absorption feature at 3.1 μm, however this is not present in diffuse interstellar clouds, including H II regions.

The chemical composition of an H II region is usually inferred from its emission spectrum. However, this only represents the gaseous abundance of elements. It is necessary to account for the fraction of a species depleted into dust in order to obtain the total abundance of an element; typically this is reported as a quantity that must be added to the gaseous abundance. The case of oxygen is particularly interesting as it is the third most abundant element in the interstellar medium. Being an interstellar shock, a Herbig-Haro object is capable of destroying dust grains, thus incorporating oxygen and other elements from the dust phase into the gas phase. Esteban et al. (1998) and Mesa-Delgado et al. (2009a) have estimated the depletion correction for oxygen to be 0.08 dex and 0.12 ± 0.03 dex respectively.

1.3 The Orion Nebula and HH202

The Orion nebula is the brightest H II region in the night sky. It is considered the standard for studying the chemical composition of H II regions and the mechanisms that play a role in the evolution of this type of objects. Herbig-Haro objects have been studied extensively in molecular clouds, where they can be observed in the infrared; however only a limited number of them have been identified and characterized in H II regions thoroughly, notably HH 529 (Blagrave et al., 2006) and HH 202 (Mesa-Delgado et al., 2009a) in the Orion nebula.

HH 202 is the brightest Herbig-Haro object discovered yet. It was first identified by Cantó et al. (1980). Its characteristics allow us to resolve and study the gas flow with high

spatial resolution. The parent star has not been identified, however the shock is expanding in a North-West direction and appears to be related to nearby Herbig-Haro objects HH 529, 203, 204, 528, 269, and 625. The kinematics of the object are well known; O'Dell & Henney (2008) report a radial velocity between -40 and -60 km/s, while Mesa-Delgado et al. (2009a) conclude that the bulk of emission comes from behind the flow. The object consists of several knots, of which the southern knot (referred to as HH202-S) is the brightest.

HH 202 has been studied previously by Mesa-Delgado et al. (2009a) with the UVES echelle spectrograph of the Very Large Telescope, and Mesa-Delgado et al. (2009b) using integral field spectroscopy. The first work is of particular interest as it presents an in-depth analysis of the physical conditions and the chemical composition of the brightest part of the shock with high precision. The high spatial resolution provided by echelle spectrophotometry enabled them to separate the emission from the static gas and the shock, and resolve individual emission lines employed for the calculation of density diagnostics, such as [O II] λ3726 and λ3729. In total, they report a total of 360 different emission lines from various ions. They also showed that the heating of the gas is due mainly to photoionization by θ^1 Ori C, effectively proving that HH 202 can be characterized as an H II region. The chemical composition of HH 202 was derived considering the presence of thermal inhomogeneities along the line of sight by means of the t^2 parameter first proposed by Peimbert (1967). Finally they calculated the amount of dust destruction and oxygen (O) depletion through different methods, which average a depletion factor of -0.12 $\pm$ 0.03 for the static gas; where the small error bars are a consequence of the quality of their observations and the data reduction process.

In general, echelle spectrographs provide higher spectral resolution than long-slit arrangements since they work with higher diffraction orders: compare for example the spectral resolution of the UVES, for which $\lambda/\Delta\lambda \approx 30\ 000$, with that of FORS 1, with $\lambda/\Delta\lambda \approx 1\ 100$. Also, UVES covers a broader wavelength range (3000 – 10400 Å) than FORS 1 (3300 – 7500 Å). Although echelle spectrographs allow for deeper studies of a particular zone of the sky, the observed area in the sky cannot be too large, otherwise the diffraction orders would overlap and the effects of astigmatism would begin to affect the observations (Chaffee & Schroeder, 1976). Indeed Mesa-Delgado et al. (2009a) observed an area of 1.5 $\times$ 2.5 arcseconds^2 of the sky covering the brightest part of HH 202-S. For this reason, a long-slit study of HH 202, which provides a larger field of view (up to 410 $\times$ 0.51 arcseconds^2 for

FORS 1), is excellent to complement the previous results and allow for the spatial exploration of parameters like chemical composition, electron density and temperature. Even if the spatial resolution of a long-slit spectrograph does not compare to that of an echelle, it still provides the opportunity to observe the brightest emission lines and compute the chemical abundance of elements such as oxygen and iron, which are relevant to estimate the amount of dust destruction by the shockwave of HH 202.

1.4 Goals and motivation

Being the brightest Herbig-Haro object in an H II region, HH 202 can provide key information about the influence of shocks in the interstellar medium. The velocity of its shockwave possesses enough energy to destroy the interstellar dust grains, releasing ions contained within; we will focus on oxygen and iron for this work, due to the important role these elements play in the chemical evolution of the universe. Since HH 202 is located in the Orion Nebula, we can analyze its composition with high spatial resolution. The concrete goals of this work are the following.

- To identify the ions present in the gas from all of the observed emission lines.
- To identify the zone at which the shock is more promiment from the intensity of the hydrogen recombination lines, determining in the process if this region coincides with the maximum dust destruction.
- To estimate the electron density and temperature of the gas, and its behavior across HH 202 and the surrounding gas of the Orion Nebula using the available diagnostics.
- To derive the chemical composition of the gas across HH 202, identifying any changes in ion abundance, in order to determine the amount of iron and oxygen released by the shock due to the destruction of interstellar dust.
- To estimate the necessary correction to account for the quantity of oxygen depleted into dust.
- To characterize the behavior of thermal inhomogeneities in the observed zones, and its impact on abundance determinations.

Chapter 2

Theory

2.1 Photoionization-recombination equilibrium

When a diffuse gas cloud is illuminated by ultraviolet photons from a hot star or star cluster, it becomes an emission nebula due to the photoionization of its gas. The ionization equilibrium at each point in the nebula is fixed by the balance between photoionizations and recombinations of electrons with ions. In a first approximation, for a pure hydrogen nebula ionized by a single star, ionization equilibrium at a point is given by

$$n(\mathrm{H}^0)\int_{\nu_0}^{\infty}\frac{4\pi J_\nu}{h\nu}a_\nu(\mathrm{H}^0)d\nu = n_e n_p \alpha(\mathrm{H}^0,T) \qquad [\mathrm{cm}^{-3}\mathrm{s}^{-1}] \tag{2.1}$$

where $n(\mathrm{H}^0)$ is the neutral hydrogen abundance, h is the Planck constant, J_ν is the mean intensity of the radiation; the integral thus represents the number of photoionizations per hydrogen atom (with ionization potential $h\nu_0 = 13.6$ eV) per unit time. The electron and proton densities are represented by n_e and n_p, and $\alpha(\mathrm{H}^0,T)$ is the recombination coefficient for neutral hydrogen. This way, photoionizations on the left-hand side of the equation are balanced by recombinations, on the right-hand side, per unit volume per unit time.

Assuming photoionization-recombination equilibrium, we can be prove that, for typical conditions in the interstellar medium, gas in H II regions is ionized by almost 100%. For a pure hydrogen nebula with a single ionizing star, the gas surrounding it adopts the shape of a sphere of fully ionized gas with a narrow (~ 0.1 pc) transition zone. This sphere is known

as the *Stromgren sphere*, with a radius gfven by

$$R_S = \left[\frac{3S_*}{4\pi n_H^2}\alpha(T)\right]^{1/3} \tag{2.2}$$

where S_* is the rate of ionizing photons. A more realistic scenario requires the inclusion of the most abundant elements such as helium (He), oxygen (O), and nitrogen (N).

The electrons produced by photoionization have an initial distribution of energies that depends on $J_\nu a_\nu / h\nu$, with a_ν the photoionization cross-section. However, the cross-section for elastic scattering collisions between electrons is about 10^{-13} cm^2; larger than a_ν, and these collisions tend to set up a Maxwell-Boltzmann energy distribution. Therefore all collisional processes occur at rates fixed by the local temperature defined by this Maxwellian.

For hydrogen, recombinations to any level n^2L quickly lead through downward radiate transitions to 1 ^2S, so the total recombination coefficient is the sum over captures to all levels, ordinarily written

$$\alpha_A = \sum_{n,L} \alpha_{n^2L}(\mathrm{H}^0, T) = \sum_n \sum_{L=0}^{n-1} \alpha_{nL}(\mathrm{H}^0, T) = \sum_n \alpha(\mathrm{H}^0, T)$$

where α_n is the recombination coefficient to all levels with principal quantum number n. It must be noted that recombinations to the ground level emit photons that are capable of ionizing another hydrogen atom. For this purpose, for an optically thick nebula it is often assumed that such photons are absorbed *on-the-spot*, that is, very close to the point at which they are generated. In the literature, the total recombination coefficient, including captures to the ground state is known as Case A; on the other hand, when we ignore said recombinations, we will refer to Case B, such that

$$\alpha_B(\mathrm{H}^0, T) = \alpha_A(\mathrm{H}^0, T) - \alpha_1(\mathrm{H}^0, T) = \sum_2^\infty \alpha_n(\mathrm{H}^0, T).$$

The physical meaning is that in optically thick nebulae, the ionizations caused by the stellar radiation field photons are balanced by recombinations to excited levels of H, while recombinations to the ground level generate ionizing photons that are absorbed elsewhere in the nebula but have no net effect on the overall ionization balance.

2.2 Temperature determinations

When we study the spectra of H II regions, it is inconvenient to work with single emission lines since the intensity of a line depends on several factors upon which the observer has no control at all, such as the distance of the object, or the thickness of the cloud. For this reason, astronomers work with emission line ratios, observing the relative behavior of two or more emission lines.

The electronic temperature in an H II region is established by the equilibrium between the heating due to photoionization, and cooling due to radiative recombination and radiation by collisionally excited lines. Some ions emit lines that are particularly useful for calculating the electronic temperature. One of the better understood ions present in H II regions is O^{2+}, whose λ4363, λ4959, and λ5007 emission lines provide one of the most widely used temperature diagnostics. These lines are emitted by levels that can be excited by electron collisions, but they have considerably different excitation energies. The [O III] λ4363 is produced by the upper level ^1S level, whereas λ 4959 and λ 5007 are emitted from the intermediate ^1D level (see Figure 2.1).

In the low-density limit, every excitation to the $^1D_2$ level results in the emission of a λ 4959 or λ 5007 photon, with the latter being three times as likely as the former. On the other hand, every excitation to the ^1S level is followed by emission of a λ 4363 or λ 2321 photon; the latter cannot be observed from the surface of the Earth, but its intensity can be inferred as it is proportional to that of λ 4363.

For these ions, the statistical equilibrium is given by

$$\sum_{m>l} n_m A_{m,l} + n_e \sum_{m\neq l} n_m q_{m,l}(T) = n_l \left[\sum_{m<l} A_{l,m} + n_e \sum_{m\neq l} q_{l,m}(T) \right], \tag{2.3}$$

where $A_{m,l}$ is the Einstein coefficient for spontaneous transition, $q_{m,l}(T)$ are the radiative excitation ($m < l$) or de-excitation ($m > l$) coefficients. For $m > l$, these coefficients are given by

$$q_{m,l}(T) = \frac{8.629 \times 10^{-6}}{T^{1/2}} \frac{\Omega_{ml}(T)}{g_m}, \tag{2.4}$$

where g_m is the statistical weight of the level at which the transition begins, and Ω_{ml} is the collision strength . The collisional excitation coefficients (i.e. $l \rightarrow m$ with $m > l$) are given

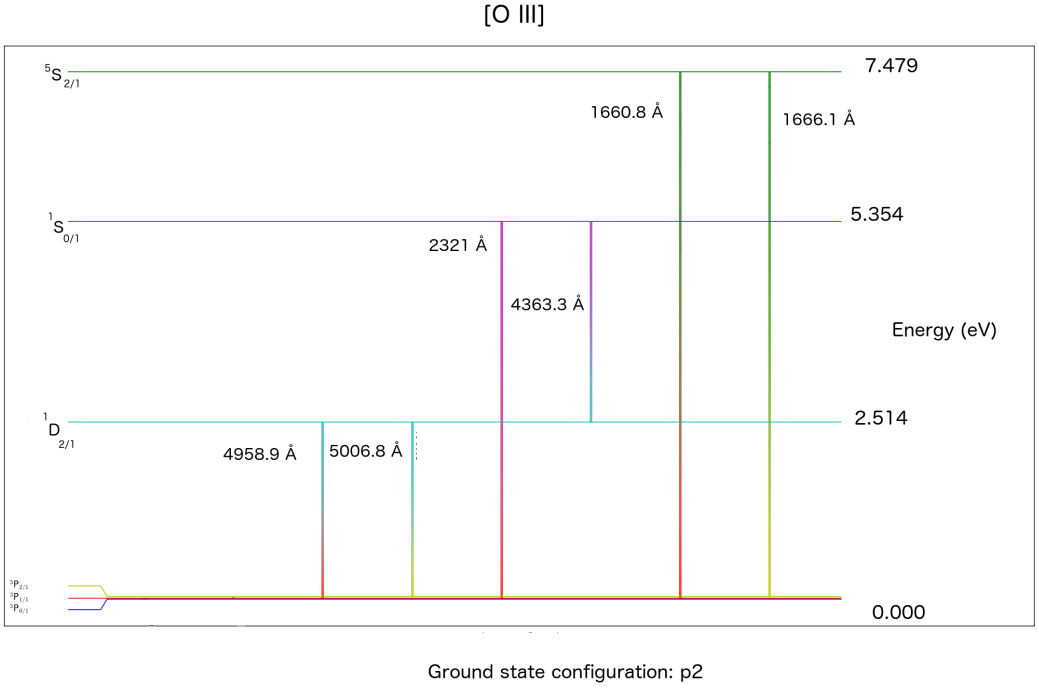

Figure 2.1: Grotrian diagram for O^{2+}.

by

$$q_{l,m}(T) = \frac{g_m}{g_l} e^{-h\nu_{m,l}/kT} q_{m,l}(T). \tag{2.5}$$

For a three-level atom the preceding equations can be solved, obtaining the relative populations of levels 3 and 2:

$$\frac{n_3}{n_2} = \left[\frac{A_{21} g_2 T^{1/2}/(n_e C\Omega_{12}) + 1}{A_{31} g_3 T^{1/2}/(n_e C\Omega_{13}) + 1}\right] \frac{g_3}{g_2} e^{-E_{23}/kT}, \tag{2.6}$$

with C a constant.

For an optically thin gas, the ratio of the intensities of the lines corresponding to transitions from level 3 to 1, and 2 to 1 are given by

$$\frac{I_3}{I_2} = \frac{n_3 A_{31} E_{31}}{n_2 A_{21} E_{21}} = \left[\frac{A_{21} g_2 T^{1/2}/(n_e C\Omega_{12}) + 1}{A_{31} g_3 T^{1/2}/(n_e C\Omega_{13}) + 1}.\right] \frac{g_3}{g_2} e^{-E_{23}/kT} \frac{A_{31} E_{31}}{A_{21} E_{21}}. \tag{2.7}$$

Finally, we can assume an electronic density n_e and estimate T_e from ratio of line intensities obtained from the observations. For the case of [O III], equation 2.7 becomes

$$\frac{I_{\lambda 4959} + I_{\lambda 5007}}{I_{\lambda 4363}} = \frac{7.9 \exp(3.29 \times 10^4/T_e)}{1 + 4.5 \times 10^{-4} n_e/T_e^{1/2}}. \tag{2.8}$$

The behavior of λ4363 / λ5007 versus T_e can be seen in Figure 2.2.

Every electronic temperature represents the zone of the nebula where the corresponding ion is located. Generally, it is assumed that ions with similar ionization potentials, such as O^{2+} and Ar^{2+}, or O^{+} and S^{+}; occupy the same volume in the nebula, therefore, usually two zones are defined: low-ionization and high-ionization, each with a corresponding temperature.

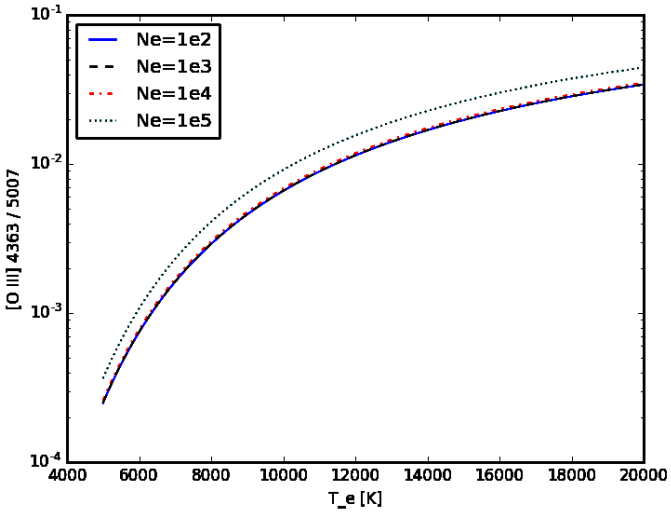

Figure 2.2: Behavior of [O III] $I(\lambda4363)/I(\lambda5007)$ ratio as a function of electron Temperature T_e.

2.3 Electron density

Just like temperature, the local electron density can be estimated by measuring the relative strength of two emission lines. For this effect, we compare two lines emitted from the same ion, originating from atomic energy levels with similar excitation energy., to avoid electron temperature effects on the population. Thus if $E_{ab} \ll kT$, for a 3-level atom, Equation 2.7 reduces to

$$\frac{I_3}{I_2} = \frac{I_3}{I_2} = \frac{n_3 A_{31} E_{31}}{n_2 A_{21} E_{21}} = \left[\frac{A_{21} g_2 T_e^{1/2}/(n_e C \Omega_{12}) + 1}{A_{31} g_3 T_e^{1/2}/(n_e C \Omega_{13}) + 1}\right] \frac{\Omega_{13} A_{31} E_{31}}{\Omega_{12} A_{21} E_{21}}. \tag{2.9}$$

After the emission line ratio has been determined observationally, one can assume an electronic temperature representative of H II regions and refer to Equation 2.9 to estimate the

electron density. If the observational data allows, it is possible to determine the intersection of the T_e and n_e values that represent the emission lines observed.

The most prominent line ratios used for this purpose in the optical range are [S II] λ6716/λ6731 and [O II] λ3726/λ3729 (see Figure 2.3) for densities up to $\approx 10^4$ cm^{-3}. In the low-density limit collisional de-excitations are negligible, and the line ratio depends on the ratio of the statistical weight of the levels originating the lines. In the high-density limit, collisional excitation and de-excitation becomes dominant, and the level populations assume a Boltzmann distribution.

Analogous to temperature, the densities obtained are representative of the volume occupied by the ion employed in the diagnostic, and thus the low-ionization and high-ionization zones have each a corresponding electronic density.

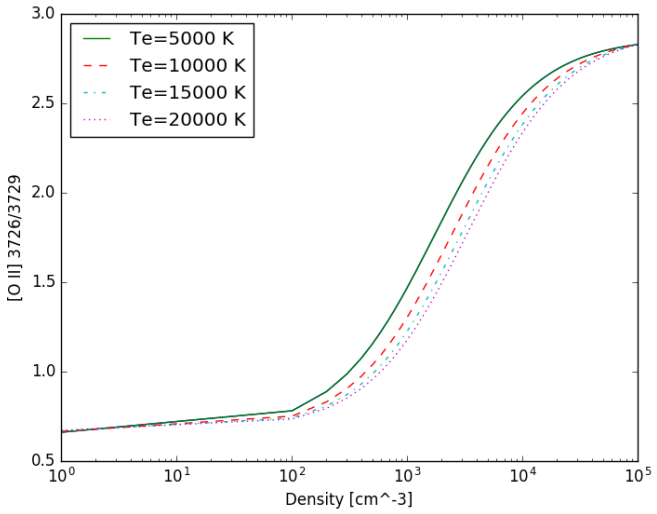

Figure 2.3: Behavior of [O II] λ 3726 / λ 3729 line ratio as a function of electron density n_e.

2.4 Chemical composition of a nebula

The abundance of the ions that make up the chemical composition of a nebula is obtained by comparing the intensity of its emission lines to those of hydrogen, more specifically to Hβ. Chemical abundances in photoionized region can be determined by two methods: by fitting

certain observed quantities through photoionization models, or using empirical methods. The latter can refer to empirical calibrations based on statistical samples, or to a direct derivation of the chemical composition, which is only possible when the physical conditions (T_e and n_e) are well known; this last method is rightfully known as the *direct method* and will be the one employed in this work given the quality of our observations.

In a gas cloud, the brightness of an emission lines is given by

$$I_l = \int j_l = \int n_i n_e \epsilon_l(T) ds \tag{2.10}$$

along the line of sight, where n_i is the abundance of the ion emitting the line, n_e is the electronic density and $\epsilon_l(T)$ represents the emission coefficient at an specific temperature.

Collisionally excited lines (CELs) emitted by heavy ions are forbidden by electric dipole selection rules and thus are also called *forbidden lines*. For these, the emission coefficient is a function that is very sensitive to temperature, so

$$I_\nu = \frac{1}{4\pi} \int n_i n_e h\nu \frac{8.63 \times 10^{-6}}{T^{1/2}} \frac{\Omega_{12}}{g_1} \exp[(-\chi)/kT] b ds \tag{2.11}$$

in the low-density limit, where b is the fraction of excitations to level 2 that are followed by emission of a photon of the line observed.

Since hydrogen is the most abundant element in the universe, ionic abundances are always reported relative to H^+. Therefore, the reported abundance of the ith stage of ionization of element X is calculated as

$$\frac{n(X^{+i})}{n(H^+)} = \frac{I(\lambda)}{I(H\beta)} \frac{j(H\beta)}{j(\lambda)}, \tag{2.12}$$

where j is the volume emissivity, which is calculated considering all of the excitation and de-excitation mechanisms. Note that reporting relative abundances also cancels the dependency on ds, the distance to the nebula.

For recombination lines, $I \propto T^{-1}$ approximately, so the ratio of two of these lines can be considered to be independent of temperature. If recombination lines of heavy elements are present in the observational data, then estimating the ionic abundance is straightforward. We must note that the recombination lines of ion X^{+i} actually are representative of the abundance of ion X^{+i+1}; e.g. the abundance of O^{2+} is inferred from O II recombination lines.

With this in mind, the relative strength of a recombination line is

$$\begin{aligned} \frac{I(\lambda)}{I(\mathrm{H}\beta)} &= \frac{\int j(\lambda)ds}{\int j(\mathrm{H}\beta)ds} \\ &= \frac{\int n_e n(\mathrm{X}^{+i+1})\alpha_{eff}(\lambda,T)ds}{\int n_e n(\mathrm{H}^+)\alpha_{eff}(\mathrm{H}\beta,T)ds} \\ &= \frac{n_e n(\mathrm{X}^{+i+1})\alpha_{eff}(\lambda,T)}{n_e n(\mathrm{H}^+)\alpha_{eff}(\mathrm{H}\beta,T)}, \end{aligned} \tag{2.13}$$

where we have assumed that density is constant along the line of sight, and that both volumes of gas are at the same distance. Solving for the ionic abundance, we obtain

$$\frac{n(\mathrm{X}^{+i+1})}{n(\mathrm{H}^+)} = \frac{\alpha_{eff}(\mathrm{H}\beta,T)}{\alpha_{eff}(\lambda,T)}\frac{I(\lambda)}{I(\mathrm{H}\beta)}. \tag{2.14}$$

Since the brightness of a recombination line depends mainly on the abundance of its parent ion, the main obstacle to working with them is that they are faint compared to CELs of heavy ions, whose emissivities are greater, and can be blended with nearby lines. Therefore only the largest telescopes, equipped with sensible detectors can resolve them with a significant signal-to-noise ratio (S/N).

The total abundance of an element is the direct sum of the abundance of all of its ions, obtained either from CELs or RLs.

Although there exists a large quantity of ions that can be observed in the visible spectrum, some emit solely in other wavelengths out of this range; thus, it is not possible to observe all ionization stages of an element examining only a restricted wavelength interval. In order to establish the total abundance of an element, one must account for the unobserved ionization stages, by means of introducing an *Ionization Corrector Factor* (ICF). ICFs are determined from similarities between ionization potentials of ions, or from photoionization models that typically involve the physical parameters of the star, the nebular conditions, and state-of-the-art atomic physics; these variables also define its range of applicability.

2.5 The abundance discrepancy problem

Collisionally excited lines were the traditional way of estimating chemical abundances until modern telescopes made it possible to work with recombination lines of heavy elements.

The first derivation of O^{2+} abundance in the Orion Nebula using RLs was reported by Peimbert et al. (1993) using data from Osterbrock et al. (1992). From these and subsequent works it was found that abundance determinations derived from CELs systematically yield a lower values than those derived from RL. This effect has been confirmed by numerous other studies as it has been observed in a large sample of H II regions and planetary nebulae. The abundance discrepancy is quantified using the abundance discrepancy factor (ADF), which, for an element X in the ith ionization stage, is defined as

$$\mathrm{ADF}(X^{+i}) = (X^{+i}/H^{+})_{RL}/(X^{+i}/H^{+})_{CEL}. \tag{2.15}$$

From studies of O^{2+} and C^{2+} abundances, authors have reported ADF values in H II regions that go from 1.3 to 2.7 (García-Rojas, 2007). In the case of planetary nebulae, similar values are found, however there are a few objects with higher ADFs, going up to $\sim$ 300. Multiple works have suggested that the physical mechanisms behind the ADF may be considerably different in H II regions and PNe. In this thesis, we will focus our attention only on H II regions.

From the discussion of the previous sections it is clear that CELs depend heavily on T_e, meaning they would be affected the most by fluctuations in temperature of any nature (or by imprecise determinations of T_e). In contrast, RLs are independent of this phenomenon; therefore, RLs are considered to yield more reliable determinations. This scenario poses the existence of thermal inhomogeneities as a possible explanation to the rise of the ADF in H II regions.

2.6 Temperature inhomogeneities

Thus far, we have assumed in our formalism that temperature is constant across the nebula. However, it is a known fact that the different methods available to determine the electronic temperature do not coincide with each other. Peimbert (1967) demonstrated that the [O III] λ 5007 + λ 4959 / λ 4363 ratio provides a higher temperature than the ratio of emission lines to the Balmer continuum of hydrogen. Therefore, temperatures derived from line ratios, or any other processes, cannot represent the object as a whole. As we have seen in previous sections, temperature is a determinant factor in the estimation of chemical abundances,

so the uncertainties associated to its derivation impact the determination of the chemical composition of H II regions.

The presence of thermal inhomogeneities in H II regions was proposed for the first time by Peimbert (1967) and Peimbert & Costero (1969), who also developed the formalism of the parameter that models them, the t^2. Numerous works have shown that incorporating this parameter makes the CEL chemical abundances agree in a considerable margin with the RL derivations, thus eliminating the ADF.

2.6.1 t^2 formalism

The intensity of a recombination line is given by

$$I_{\rm RL} = C \times \int n_i n_e T_e^{\alpha} d\Omega ds, \tag{2.16}$$

where C is a constant that depends on atomic parameters.

We can define an average temperature for each ion:

$$T_0 = \frac{\int T_e n_i n_e d\Omega ds}{\int n_i n_e d\Omega ds}. \tag{2.17}$$

However, observations provide information about the average of T^{α}, which is different from the average temperature, that is

$$\langle T^{\alpha} \rangle = \frac{\int T^{\alpha} n_i n_e d\Omega ds}{\int n_i n_e d\Omega ds} \neq \langle T \rangle^{\alpha} = T_0^{\alpha}. \tag{2.18}$$

For small temperature fluctuations, a Taylor expansion of T^{α} around T_0 gives

$$T^{\alpha} = \langle T^{\alpha} \rangle^{1/\alpha} \approx T_0 \left(1 + \frac{\alpha - 1}{2} t^2 \right). \tag{2.19}$$

t^2 is the root mean square temperature fluctuation, given by

$$t^2 = \langle \left[\frac{T - T_0}{T_0^2} \right] \rangle = \frac{\int T^2 n_e n_i d\Omega ds - T_0^2 \int n_e n_u d\Omega ds}{T_0^2 \int n_e n_i d\Omega ds}. \tag{2.20}$$

In most H II regions, higher order terms can be ignored.

In the case of a temperature derived from two powers of T, the ratio can be expressed as

$$\frac{\langle T^{\alpha} \rangle}{\langle T^{\beta} \rangle} = \frac{\int T^{\alpha} n_e n_i d\Omega ds}{\int T^{\beta} n_e n_i d\Omega dl} \approx \frac{T_0^{\alpha} \left[1 + \frac{1}{2} \alpha (\alpha - 1) t^2 \right]}{T_0^{\beta} \left[1 + \frac{1}{2} \beta (\beta - 1) t^2 \right]}, \tag{2.21}$$

so the temperature is then

$$T_{\alpha/\beta} = \left(\frac{\langle T^{\alpha}\rangle}{\langle T^{\beta}\rangle}\right)^{1/(\alpha-\beta)} \approx T_0\left(1+\frac{\alpha+\beta-1}{2}\right)t^2, \quad \alpha \neq \beta. \tag{2.22}$$

A similar treatment is given to collisionally excited lines, whose intensity is given by

$$I(\mathrm{X}^{+i},\lambda_{mn})_{\mathrm{CEL}} = C \times \int n(\mathrm{X}^{+i}) n_e A_{mn} W(\mathrm{X}^{+i},n)\frac{h\lambda_{mn}}{c} d\Omega ds, \tag{2.23}$$

where C is determined by atomic parameters, λ_{mn} is the emission wavelength, $n(\mathrm{X}^{+i})$ is the abundance of ion X^{+i}, A_{mn} is the Einstein transition coefficient, and $W(\mathrm{X}^{+i},n)$ is the fraction of atoms of X element in the $+i$ ionization stage. If collisional de-excitations are negligible, then we can rewrite Equation 2.23 as

$$I(\mathrm{X}^{+i},\lambda_{mn})_{\mathrm{CEL}} = C \times \int n(\mathrm{X}^{+i}) n_e T_e^{-1/2} exp[-\Delta E/kT_e] d\Omega ds. \tag{2.24}$$

Just as in the case of RL, we can define an average temperature for CELs:

$$\langle T(\lambda_{mn})^{-1/2} exp[-\Delta E/kT(\lambda_{mn})]\rangle = \frac{C \times \int n(\mathrm{X}^{+i}) n_e T_e^{-1/2} exp[-\Delta E/kT_e] d\Omega ds}{C \times \int n(\mathrm{X}^{+i}) n_e d\Omega ds}, \tag{2.25}$$

where ΔE is the energy difference between levels m and n.

Now, performing a Taylor series expansion around T_0 we obtain

$$I(X^{+i},\lambda_{mn}) \approx T_0^{-1/2}\left[1+T_0^{-1}\left(\frac{\Delta E}{kT}-\frac{1}{2}\right)(T(\lambda_{mn})-T_0)\right] exp[-\Delta E/kT_0], \tag{2.26}$$

with

$$T(\lambda_{mn}) = T_0\left(1+\left[\frac{(\Delta E/kT_0)^2 - 3\Delta E/kT_0 + 3/4)}{\Delta E/kT_0 - 1/2}\right]\frac{t^2}{2}\right). \tag{2.27}$$

For a line ratio we have, using Eqs. 2.26 and 2.27,

$$T(\lambda_{mn}/\lambda_{n'm'}) \approx T_0\left[1+\left(\frac{\Delta E+\Delta E'}{kT_0}-3\right)\frac{t^2}{2}\right], \tag{2.28}$$

where $\Delta E \neq \Delta E'$, and $t^2 \ll 1$.

2.6.2 Abundance determinations using t^2

Once the t^2 parameter has been introduced to account for thermal inhomogeneities, we must link the previous formalism with the abundance determinations. The relative intensity of a

line with respect to Hβ is

$$\frac{I(\mathrm{X}^{+i},\lambda_{mn})}{I(\mathrm{H}\beta)} = \frac{C \times \int n(\mathrm{X}^{+i}) n_e T_e^{-1/2} exp(-\Delta E/kT_e) d\Omega ds}{C \times \int n_i n_e T_e^{-0.827} d\Omega ds}, \tag{2.29}$$

if we assume that both emission lines originate from the same volume, then the dependency on $d\Omega$ and ds cancels. Solving for the relative abundance we have

$$\left[\frac{n(\mathrm{X}^{+i})}{n(\mathrm{H}^{+})}\right]_{t^2\neq 0.00} = C\frac{I(\mathrm{X}^{+i},\lambda_{mn})}{I(\mathrm{H}\beta)} \frac{T(\mathrm{H}\beta)^{-0.827}}{T(\lambda_{mn}^{-1/2}) exp(-\Delta E/kT(\lambda_{mn}))}. \tag{2.30}$$

This expression can be used for computing ionic abundances under constant temperature, assuming $T(\mathrm{H}\beta) = T(\lambda_{mn})$, with $T(\lambda_{mn})$ obtained through a line ratio diagnostic. For the [O III] λ4363/ λ5007 ratio we have

$$\frac{I(5007)}{I(\mathrm{H}\beta)} = C\frac{T_{(4363/5007)}^{-1/2} exp(\Delta E/kT_{4363/5007})}{T_{4363/5007}^{-0.827}} \left[\frac{n(\mathrm{O}^{2+})}{n(\mathrm{H}^{+})}\right]. \tag{2.31}$$

Substituting the line ratio from Equation 2.29 in Equation 2.31 and solving for the relative abundance, we obtain, finally

$$\left[\frac{n(\mathrm{O}^{2+})}{n(\mathrm{H}^{+})}\right]_{t^2\neq 0.00} = \frac{T(\mathrm{H}\beta)^{-0.827} T_{(5007)}^{1/2}}{T_{4363/5007}^{-0.327} exp(-\Delta E/kT_{4363/5007} + \Delta E/kT_{5007})} \times \left[\frac{n(\mathrm{O}^{2+})}{n(\mathrm{H}^{+})}\right]_{t^2=0.00}. \tag{2.32}$$

Note that in this equation $T(\mathrm{H}\beta) \neq T(\lambda_{mn}) \neq T_{4363/5007}$; the last term is still obtained directly from the line ratio, however T(Hβ) and $T(5007)$ are obtained simultaneously from T_0; $T(5007)$ is called the *line temperature*, since it represents the temperature required to reproduce the observed intensity of [O III] λ5007. Finally, Equation 2.32 can be rewritten as

$$\left[\frac{n(\mathrm{O}^{2+})}{n(\mathrm{H}^{+})}\right]_{t^2\neq 0.00} = K \left[\frac{n(\mathrm{O}^{2+})}{n(\mathrm{H}^{+})}\right]_{t^2=0.00} \tag{2.33}$$

where K is the ADF.

Chapter 3

Observations

The observations of HH 202 were carried out during the night of September 11, 2002 at the Very Large Telescope (VLT), in Cerro Paranal, Chile with the Focal Reducer and low dispersion Spectrograph (FORS 1); this is a long-slit spectrograph with a field of view of up to 6.8 arcminutes. Data were obtained from three different grism configurations: GRIS-600B+12, GRIS-600R+14 with filter GG435+31, and GRIS-300V+10 with filter GG375+30 (see Table 3.1).

An image of the Orion Nebula from our observations can be seen in figure 3.1. HH 202-S is located 46″to the North and 60″.4 to the west of θ^1 Ori C [1], which is the brightest star of the Trapezium; this corresponds with a difference in hour angle of 4.01 seconds. The slit was oriented North–South, and the atmospheric dispersion corrector was used to keep the same observed region within the slit regardless of the airmass value. The slit length was 410″and the width was set to 0.51 ″. This setting was chosen to have the resolution to deblend the [O II] λ3726 and λ3729 emission lines, as well as measuring O II λ4642 and λ4650 with a significant signal to noise ratio with GRIS-600B+12.

The final spectrum was reduced using IRAF[2] following the standard procedure of bias substraction, aperture extraction, flat fielding, wavelength calibration and flux calibration.

[1]The coordinates of θ^1 Ori C for J2000 are $\delta = -05^\circ 23' 22''.8486$ $\alpha = 05^h 35' 16''.46375$

[2]IRAF is distributed by National Optical Astronomy Observatories, which is operated by the Association of Universities for Research in Astronomy, under cooperative agreement with the National Science Foundation).

Grism	Filter	λ (Å)	Resolution ($\lambda/\Delta\lambda$)	Exposure time (s)
GRIS-600B+12	$\cdots$	3450–5900	1300	3×60
GRIS-600R+14	GG435	5250–7450	1700	5×30
GRIS-300V	GG375	3850–8800	700	3×20

Table 3.1: Journal of observations

The standard stars used for this purpose were LTT 2415, LTT 7389, LTT 7987, and EG 21 (Hamuy et al., 1992, 1994). The error in flux calibration has been estimated to be 1%; the contribution to the errors due to the noise was estimated from the continuum. Other objects observed throughout the night were NGC 456 and 460 in the Small Magellanic Cloud (SMC) (Peña-Guerrero et al., 2012); and TOL 2146391 and TOL 03573915 (Peimbert et al., 2012).

In order to analyze the spatial variations of the physical properties and of the chemical abundances 54 extraction windows were defined. Windows North and South of HH202-S span 50 pixels (10 ″) each, whereas those covering the object are 3 pixels (0.6 ″) long each. This treatment of the data allowed us to establish the composition of the Herbig-Haro object and compare it directly with the surrounding gas of the Orion nebula. An spectrum of the brightest part of HH 202 is presented in Figure 3.2, showing the lines of multiplet 1 of O^{2+}.

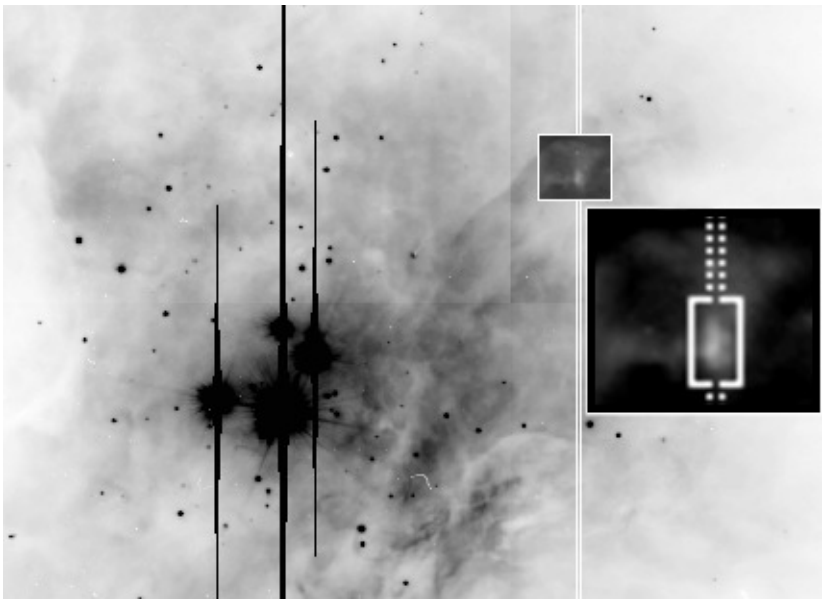

Figure 3.1: Central part of the Orion Nebula. The white vertical lines show the position and width of the slit used. The region inside the white box represents HH202-S. A close-up image of the shock is also shown; the white rectangle encloses the zone with the peak of emission of Hβ, [Fe II] λ7155, and [Fe III] λ4658. North points to the top of the image and East to the left.

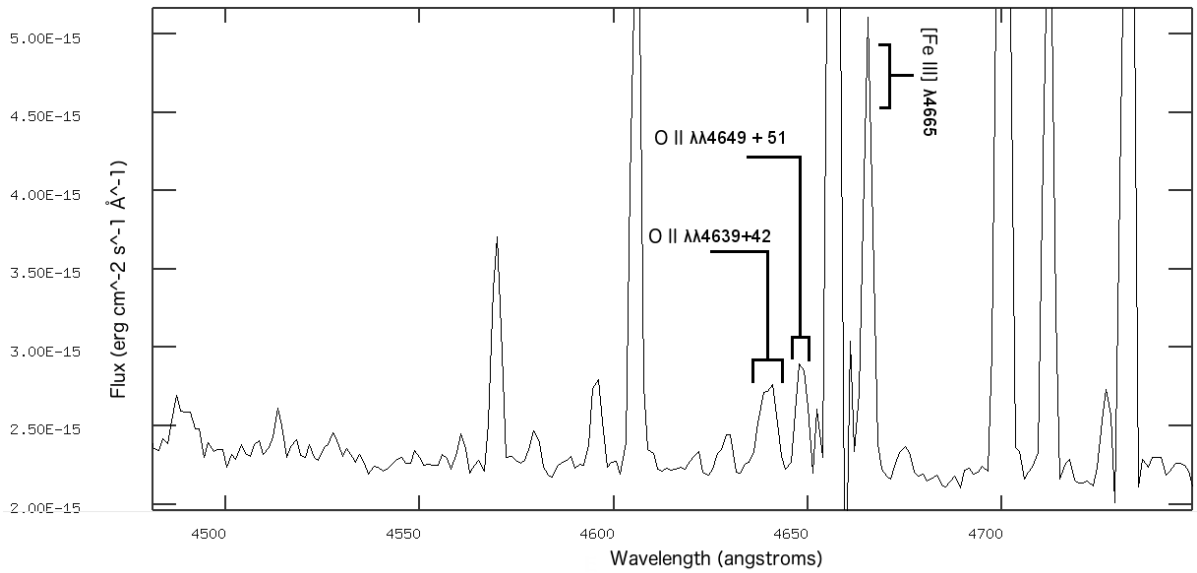

Figure 3.2: Spectrum of the central part of HH 202, showing the lines of multiplet 1 of O^{2+}.

Chapter 4

Data analysis

The 54 extraction windows described in the previous chapter were analyzed using the SPLOT routine of IRAF. First, we performed an analysis on each individual spectrum covering both HH 202 and the surrounding gas of the Orion Nebula with the intention of identifying the spatial variation in physical conditions across the observed area. This procedure served as a basis to perform a deeper study combining several spectra representative of the shock and the static gas.

4.1 Spatial analysis

We performed an analysis of the flux of a set of emission lines on all 54 windows: the Balmer series up to H9; [Fe II] λ7155; [Fe III] λ4658; and O II λ4640 and λ4652. The flux of the emission lines was determined by integrating between two points over the local continuum estimated by eye. A Gaussian profile was fitted to the lines that were blended (such as [O II] $\lambda\lambda$3726 and 3729), using IRAF's SPLOT routine: the laboratory wavelength separation was taken as reference, while allowing the actual wavelength to shift while keeping the separation constant; both lines were also considered to have the same width.

The flux of Hα is presented in Figure 4.1 showing a peak that coincides perfectly with the brightest section of the slit covering the object (Figure 3.1). This also coincides with the peak of the iron emission lines presented in Figure 4.2; indicating the center of the shock.

Noise flux was estimated by averaging direct measurements from different parts of the spectrum where emission lines were absent. Using this procedure we estimated the signal to noise ratio and the percentage error associated to the intensity of every emission line.

Emission lines had to be corrected for interstellar extinction caused by interstellar dust, which absorbs and scatters radiation coming from the stars and gas. Extinction as a function of wavelength is given by

$$E(\lambda) = 10^{-C(\mathrm{H}\beta[1+f(\lambda)])} \tag{4.1}$$

where $f(\lambda)$ is adjusted so that $f(\mathrm{H}\beta) = 0$; $C(\mathrm{H}\beta)$ is the logarithmic extinction in Hβ, which was fit manually.

When analyzing emission spectra, we must not forget that the radiation continuum is dominated by stars. Stellar spectra typically show the presence of absorption lines of H and He; so the presence of stars in the nebula can modify the observed gas emission. This phenomenon is known as underlying absorption and has to be corrected before estimating the physical conditions of the gas.

Interstellar extinction and underlying absorption were corrected simultaneously according to Equation 4.2:

$$\frac{I(\lambda)}{I(\mathrm{H}\beta)} = \frac{F(\lambda)}{F(\mathrm{H}\beta)} 10^{f(\lambda)C(\mathrm{H}\beta)} \left(1 - \frac{\mathrm{EW_{abs}}(\lambda)}{\mathrm{EW}(\lambda)}\right) \left(\frac{1}{1 - \frac{\mathrm{EW_{abs}}(\mathrm{H}\beta)}{\mathrm{EW}(\mathrm{H}\beta)}}\right) \times \frac{100}{\eta}; \tag{4.2}$$

where $F(\lambda)$ is the absolute flux, observed for each line; η modifies the value of Hβ; EW(λ) is the observed equivalent width of an emission line; and EW$_{abs}(\lambda)$ is the theoretical equivalent width respect to that of Hβ.

As we can see, when correcting for extinction and underlying absorption, the only free parameters are $C(\mathrm{H}\beta)$ and EW$_{abs}$(Hβ). These parameters were fitted simultaneously, comparing the observed $I(\lambda)$ for hydrogen lines with those from Storey & Hummer (1995).

We tested the extinction laws of Seaton (1979), Cardelli et al. (1989), and Costero & Peimbert (1970). The reddening correction for Hβ, $C(\mathrm{H}\beta)$, and the underlying absorption were fitted simultaneously to the theoretical ratios. The theoretical intensity ratios for the Balmer emission lines were calculated using INTRAT by Storey & Hummer (1995) considering a constant electronic temperature $T_e = 9000$ K, and an electronic density $n_e = 5000$ cm^{-3}; there was no need to modify these values since hydrogen lines are nearly independent

from temperature and density. The underlying absorption ratios for the Balmer and helium emission lines were taken from Table 2 of Peña-Guerrero et al. (2012). The most suitable values for $C(\mathrm{H}\beta)$ and the underlying absorption in Hβ, $\mathrm{EW_{abs}}(\mathrm{H}\beta)$, were found by reducing the quadratic discrepancies between the theoretical and measured H lines in units of the expected error, χ^2, defined as

$$\chi^2 = \sum_{i=1}^{n} \left(\frac{I(\lambda)_{\mathrm{obs}} - I(\lambda)_{\mathrm{teo}}}{I(\lambda)_{\mathrm{teo}}} \times \frac{1}{\%\mathrm{err}(I(\lambda))/100} \right)^2, \tag{4.3}$$

where $I(\lambda)_{\mathrm{obs}}$ is the intensity of a line after being corrected for extinction and underlying absorption; $I(\lambda)_{\mathrm{teo}}$ is the theoretical intensity from the literature, and $\%\mathrm{err}(I(\lambda))$ is the percentage uncertainty.

The extinction law by Costero & Peimbert (1970) delivered the most satisfying results and is the one we adopted for the rest of this work. The fluxes were normalized with respect to the whole Balmer decrement, meaning that the value of Hβ was allowed to deviate slightly from 100.

The brightest section of HH202-S was identified to have coordinates (J2000.0) $\alpha = 05^h35^m11^s.6$, $\delta =$ -5°22′56″. The former was determined from the peak of emission of [Fe II] λ7155; [Fe III] λ4658; O II $\lambda\lambda$4640 and 4652; and Hα.

The emission line intensities for [Fe II] λ7155 and [Fe III] λ4658 are presented in Figure 4.2. We can see how the intensities of both lines increase by an order of magnitude for a region about 4 arcseconds in length. To confirm that the observed increase in intensity cannot be explained by differences in temperature or density, we calculated the expected [Fe III] λ4658 / [O III] λ5007 emissivity for a range of n_e and T_e using PyNeb (see Figure 4.3): the relative emissivity of these two lines presents no abrupt changes for the conditions considered; if we examine I([Fe III] λ4658)/I([O III]λ5007), presented in Figure 4.4, whose dependency includes ion abundance, we conclude that only an increase in Fe^{2+}/ H^+, due to the incorporation of iron to the gaseous phase after the destruction of interstellar dust in a considerable scale. We will define the zero point in our coordinates as the one corresponding to maximum [Fe II] and [Fe III] intensities.

Electron temperatures, T_{e}, and densities, n_{e}, across the area of the Orion Nebula covered by the slit are presented in Figures 4.5 and 4.6. The [N II] λ 6584/ λ 5755 and [O II] λ 5007/ λ 4363 ratios were used to determine the low- and high-ionization temperatures. For density,

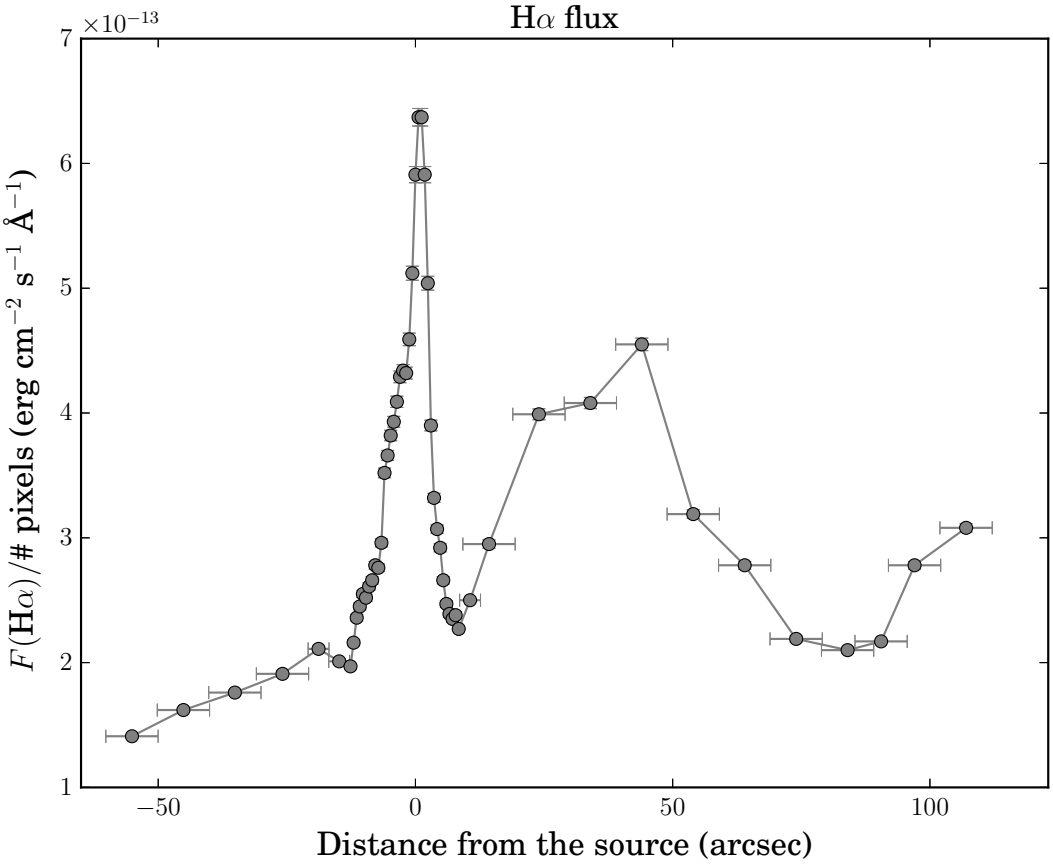

Figure 4.1: Hα flux across the Orion Nebula. The zero mark was determined from the peak of [Fe III] emission with approximate coordinates $\alpha = 05^h35^m11^s.6$ and δ = -5°,22′,56″.2 (2000). North is to the left of the zero mark and South is to the right.

we computed the average of the [S II] λ 6716/ λ 6731, and [Cl III] λ 5517/ λ 5537 ratios since the uncertainties associated to the latter one were of a considerable size. We did not take into account the[O II] λ3726 / λ3729 density diagnostic since both lines are blended in our spectra, and deblending them would introduce uncertainties that may be considerably larger than the ones estimated from the [S II] diagnostic. The references for the atomic data set used to compute physical conditions and chemical abundances are presented in Table 4.1.

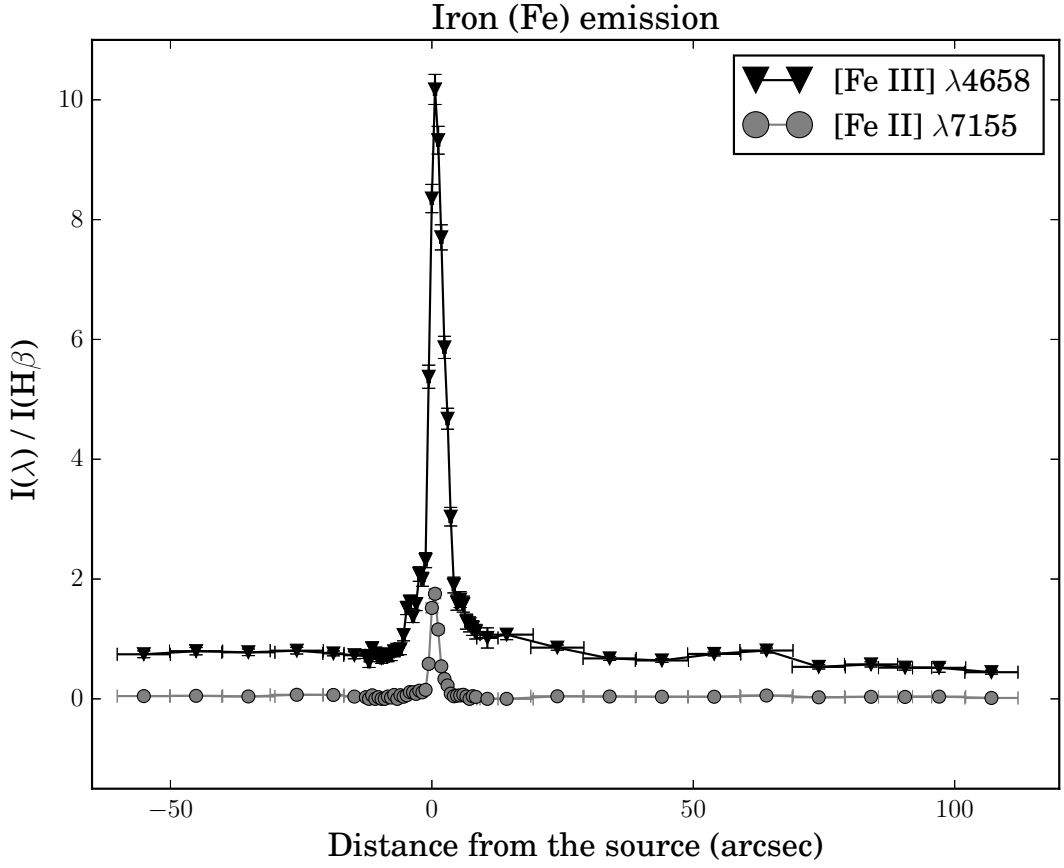

Figure 4.2: Dereddened emission line intensities for [Fe II] λ7155 and [Fe III] λ4658 across the Orion Nebula.

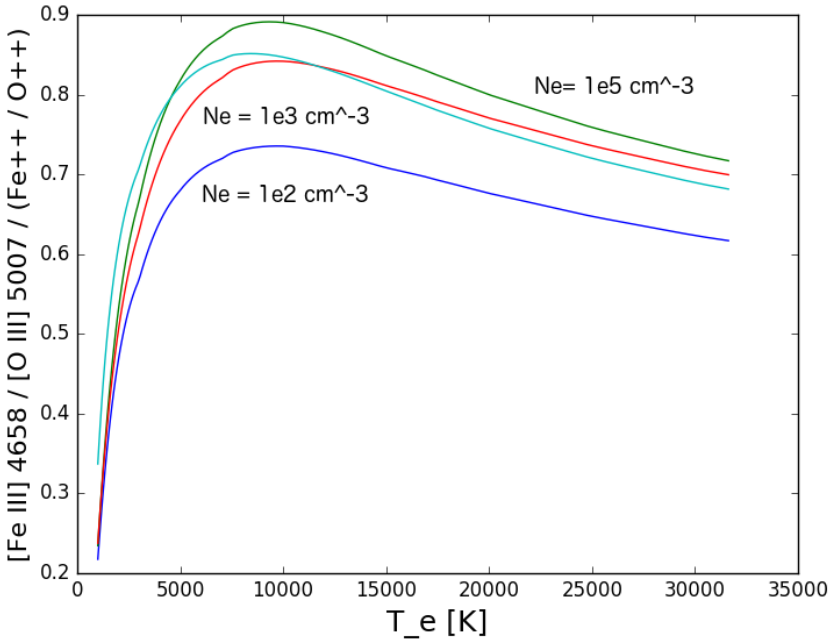

Figure 4.3: [Fe III] λ4658 / [O III] λ5007 emissivity.

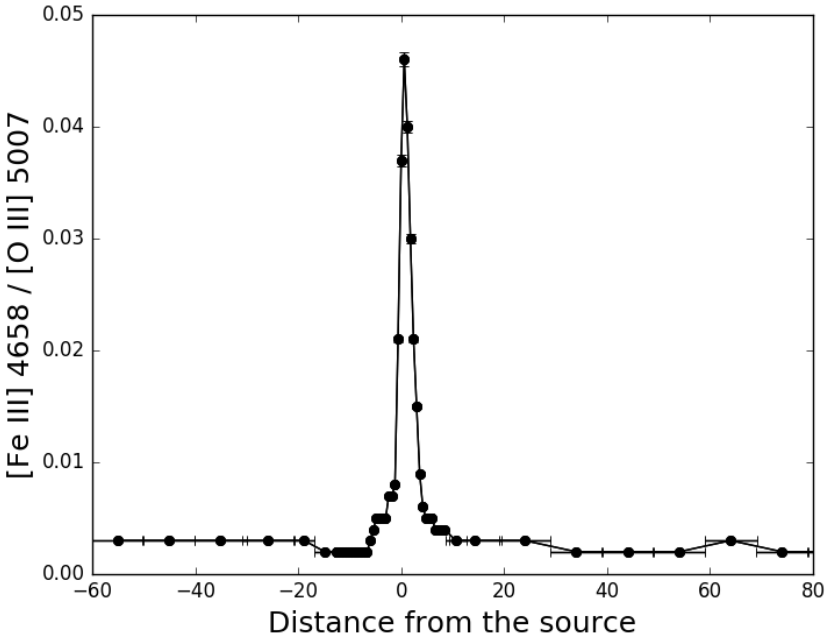

Figure 4.4: Observed I([Fe III] λ4658)/I([O III] λ5007).

The physical conditions reported here were obtained using PyNeb (Luridiana et al., 2015), by identifying the intersection of the corresponding temperature and density diagnostics. Our results for the North and South zones away from the shock agree with previous determinations made by Rubin et al. (2003), Esteban et al. (2004) and Mesa-Delgado et al. (2009a). In the case of the shocked spectra, our results agree within 1-σ with the reported [N II] and [O III] electron temperature by Mesa-Delgado et al. (2009a), also with the [Cl III] and [O II] densities. We attribute this difference to the fact that in our study we are observing a volume of gas which contains both shocked and unshocked gas, both of which contribute to the observed emission; also, differences in flux calibration and the extinction law used may cause these little disparities; however, this does not have heavy implications on the chemical abundances since the dependency of an emission line intensity with $n_{\rm e}$ is minimal; moreover, oxygen recombination lines, which will be central to our analysis, have a negligible dependency with temperature.

We computed the total abundance for oxygen in two ways: from CELs and RLs. The abundance from CELs, $O_{\rm CEL}$, is the sum of the O^+/H^+ and O^{2+}/H^+, obtained from [O III] λ5007 and [O II] λ3726+29 respectively. For the RL oxygen abundance we have used multiplet 1 of O II to determine O^{2+}/H^+. The intensity of multiplet 1 of O II is the sum of eight lines, of which we only detected four blended in pairs as $\lambda\lambda4639 + 42$ and $\lambda\lambda4649 + 51$. The total intensity was estimated considering the dependence on density and temperature of the lines, according to the work of Peimbert & Peimbert (2010). The effective recombination coeficients were taken from Storey (1994) for case B, assuming $n_{\rm e} = 10,000$ cm^{-3}. Although O I lines are present in our spectra, they are contaminated by telluric emission, making them unreliable for calculating O^+/H^+; to account for O^+/H^+ we assume the following relation between O^+ and O^{2+}:

$$\left[\frac{\rm O}{\rm H}\right]_{\rm RL} = \left[\frac{\rm O^{2+} + O^{+}}{\rm O^{+}}\right]_{\rm CEL} \times \left[\frac{\rm O^{2+}}{\rm H^{+}}\right]_{\rm RL} \tag{4.4}$$

Esteban et al. (2004) also favor the former procedure. Oxygen abundances derived from RLs and CELs are presented in Figure 4.7. While small, there is a significant difference between the oxygen abundance near the apex of HH202-S compared with the surrounding —presumed static— gas; it is also evident from Figure 4.7 that $O_{\rm CEL}$ and $O_{\rm RL}$ are irreconcilable in the line of sight of the shock. In other words, the Abundance Discrepancy Factor is greater at the brightest zone of HH 202; this occurrence had been reported before in HH 202 and other

Herbig-Haro objects of the Orion Nebula by Mesa-Delgado et al. (2008).

Away from the center, the difference between O_{RL} and O_{CEL} is much smaller, about 0.1 dex in size. In their study of planetary nebula IC 418, Escalante et al. (2012) found that O II emission lines of multiplet 1 could be affected by fluorescence, making the expected intensity due to recombination lower by 25 %. Although the physical conditions in the Orion Nebula and IC 418 are similar —the central star of IC 418 has an effective temperature of 36 700 K compared to 39 000 K of θ^1 Ori C; also the gas electron temperature in IC 418 has been modeled to be 8375 K, with an electron density of 2700 cm^{-3}—, the planetary nebula has a higher O^+ / H^+ content than M42, and since this ion is the one responsible for fluorescence, its effects may have a lower contribution to the multiplet 1 emission in our study. Nonetheless, the impact of fluorescence on this ion has not been analyzed quantitatively in H II regions; an exploration on this subject using detailed photoionization models would be ideal for this, a good candidate for such a study would be M43, which presents a simpler geometry than the Orion Nebula.

It is known that oxygen is present in interstellar dust grains in the form of water ice and metallic compounds such as FeO, CaO and MgO (Draine, 2011). Theoretical and empirical studies have shown that dust can be destroyed by grain-grain collisions in interstellar shocks —a process known as sputtering— thus reincorporating refractory elements into the diffuse gas, however these studies have been carried out mostly in molecular clouds (see, for example Podio et al. (2009) and references therein) and supernova remnants (Gall et al., 2014), (Mouri & Taniguchi, 2000). Dust composition in H II regions is known to be different from that found in molecular clouds due to photo-evaporation of ice molecules by UV radiation; in any case the relation between dust destruction and shock velocity is not entirely clear. The only work to study dust destruction in a Herbig-Haro object in an H II region and its effect on oxygen was made by Mesa-Delgado et al. (2009a) who also examined HH202-S, finding an increase in oxygen, iron and magnesium abundance at the shock; showing the presence of dust destruction in the aftermath of moderate shockwaves. This effect is also present in our observations.

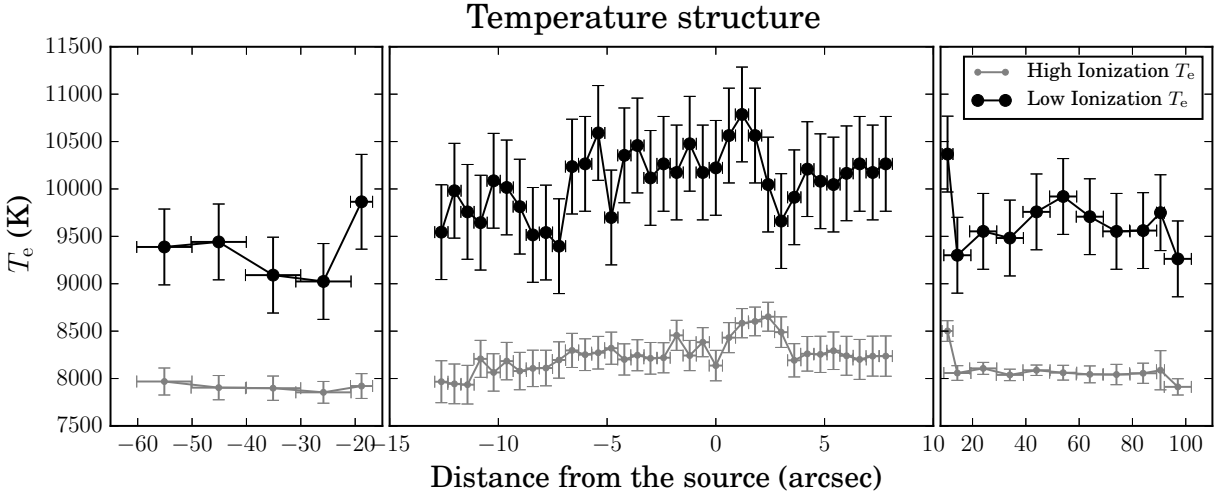

Figure 4.5: Temperature structure: The low-ionization temperature corresponds to [N II] $\lambda\lambda$ 5755/6584; the high-ionization temperature was calculated using [O III] $\lambda\lambda$ 4363/5007.

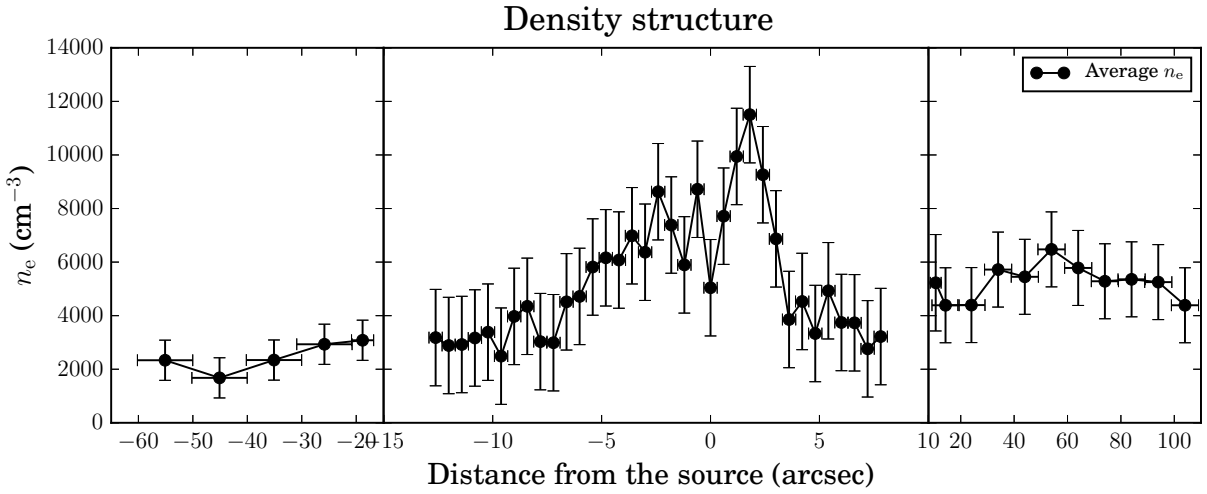

.

Figure 4.6: Density structure: Density shown is an average of the [S II] $\lambda\lambda$ 6716/6731 and [Cl III] $\lambda\lambda$ 5518/5538 diagnostics

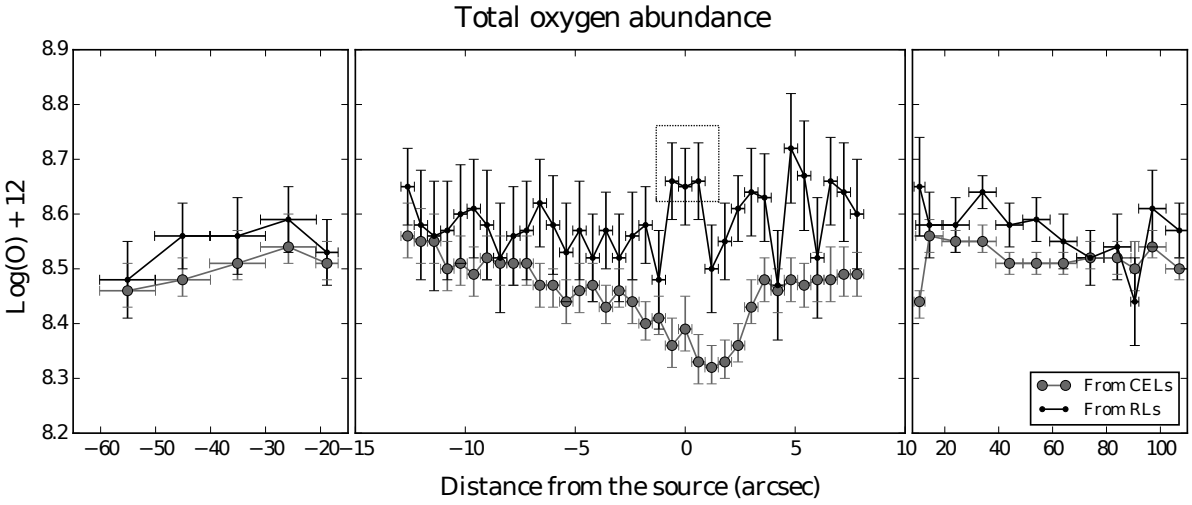

Figure 4.7: Total oxygen abundance computed using CELs and O II RLs (see text). Note that the difference is maximum at the apex of the shock.

Ion	Transition probabilities	Collision strengths
N^{+}	Wiese et al. (1996) Galavis et al. (1997)	Tayal (2011)
O^{+}	Wiese et al. (1996), Pradhan et al. (2006)	Tayal (2007)
O^{2+}	Wiese et al. (1996), Storey & Zeippen (2000)	Aggarwal & Keenan (1999)
S^{+}	Mendoza & Zeippen (1982)	Tayal & Zatsarinny (2010)
S^{2+}	Mendoza & Zeippen (1982)	Tayal & Gupta (1999)
Cl^{2+}	Mendoza (1983)	Butler & Zeippen (1989)
Ar^{2+}	Mendoza (1983)	Galavis et al. (1995)
Fe^{2+}	Quinet (1996), Johansson et al. (2000)	Zhang (1996)
Ni^{2+}	Bautista (2001)	Bautista (2001)

Table 4.1: Atomic data set

4.2 Analysis from combined spectra

In order to enhance the signal-to-noise ratio and reduce the possible uncertainties produced by measuring very weak lines we decided to combine the three spectra with the highest Fe abundance (the ones with maximum dust destruction), which we will call the strongly shocked zone (SS). To represent the static gas we chose two regions: one averaging 4 windows 20 arcseconds south of HH 202-S (south zone), and one averaging 4 regions 20 arcseconds north of HH 202-S (north zone). Finally we also combined the spectra of four weakly shocked zones (WS). The resulting spectra were studied in detail for this section.

The extinction correction for Hβ corresponding to the extinction law of Costero & Peimbert (1970) are presented at the bottom of Table 4.3.

The emission line intensities for the four combined spectra covering Northern and Southern zones of the Orion Nebula as well as HH202-S are presented in Table 4.3 in columns 4–11. Column 1 shows air the laboratory wavelength λ; column 2 presents the identification for each line based on the work by Esteban et al. (2004) and the Atomic Line List v2.04[1]; column 3 presents the value of $f(\lambda)$ for each line. Overall, we have identified 169 different emission lines in our combined spectra; the Strongly Shocked Zone shows the most emission lines, with 159, including several additional [Cr II] and [Fe II] lines.

The error associated to every emission line was determined from the flux of the weakest lines; by identifying the value at which they became dominated by noise, we estimated a flux value that was representative of 3σ significance over the noise in every window, which is presented in Table 4.2. Thus, the percentage error reported in table 4.3 is calculated as

$$\%err = 100 \times \sqrt{\frac{F_0}{F(\lambda)}(0.33^2) + (0.01)^2} \tag{4.5}$$

where the $(0.01)^2$ term is due to the estimated error in flux calibration, and F_0 is the corresponding flux for a 3σ detection.

From Table 4.3 and Figure 4.3 we can ascertain that dust is being destroyed by the shock front. Comparing the intensity of the iron emission lines in the strongly shocked zone with an average for the North and South zones we find that all of them are brighter at the apex of HH202-S; particularly, [Fe II] λ7155 is 26 times more intense at the shock and [Fe III]

[1]The Atomic Line List is maintained by Peter van Hoof: http://www.pa.uky.edu/ peter/atomic/.

Wavelength interval	North Zone	South Zone	Weakly Shocked Zone	Strongly Shocked Zone
3500 - 5500 Å	1.49E-15	7.13E-15	5.59E-16	9.42E-16
5500 - 7500 Å	1.25E-15	3.67E-15	4.34E-16	5.20E-16

Table 4.2: 3σ flux values (erg cm^{-2} s^{-1} Å^{-1})

λ4658 is 13 times brighter. The increase in the gaseous abundance at the shock is due to the incorporation of this iron by the destruction of dust grains.

As stated in Chapters 1 and 2, the spectral resolution of FORS 1 does not allow us to separate the purely shocked gas from the unshocked component in the WS and SS zones. Also, we cannot use the North and South zones as 'background' spectra since, even in the zones where the gas is assumed to be static (see Figure 4.1), the brightness of emission lines is not constant across the observed area of M42.

4.2.1 Physical conditions

We computed diagnostics for $T_{\rm e}$ and $n_{\rm e}$ using using PyNeb. For high ionization we used [O III] λ 4363/ λ5007, and [Ar III] λ5192 / λ7136 for T_e, and [Cl III] λ5518 / λ5538 for n_e; for low ionization we computed [N II] λ5755 / $\lambda\lambda$6548 + 84, [O II] $\lambda\lambda$3726 + 29 / $\lambda\lambda$7319 + 30, [S II] $\lambda\lambda$4069 + 76 / $\lambda\lambda$6716+31 for T_e; and [O II] λ3726 / λ3729, [S II] λ6716 / λ6731 for n_e. These diagnostics are presented in Figure 4.8; the depicted confidence intervals are calculated from the root-mean-squared error of the corresponding emission lines. The high ionization temperature and density were determined from the intersection of the [O III] and [Cl III] diagnostics. For low ionization, the physical conditions were determined graphically from the available diagnostics (see the aforementioned figures) by establishing the midpoint between the [N II], [O II], and [S II] lines. Table 4.5 presents the specific physical conditions for each diagnostic as well as the adopted $T_{\rm e}$ and $n_{\rm e}$. As we can see from Figure 4.8, the [O II] and [S II] temperature diagnostics are unreliable for computing the low-ionization electron temperature (the results of the computation are presented in Table 4.5), and thus were ignored for the rest of the analysis.

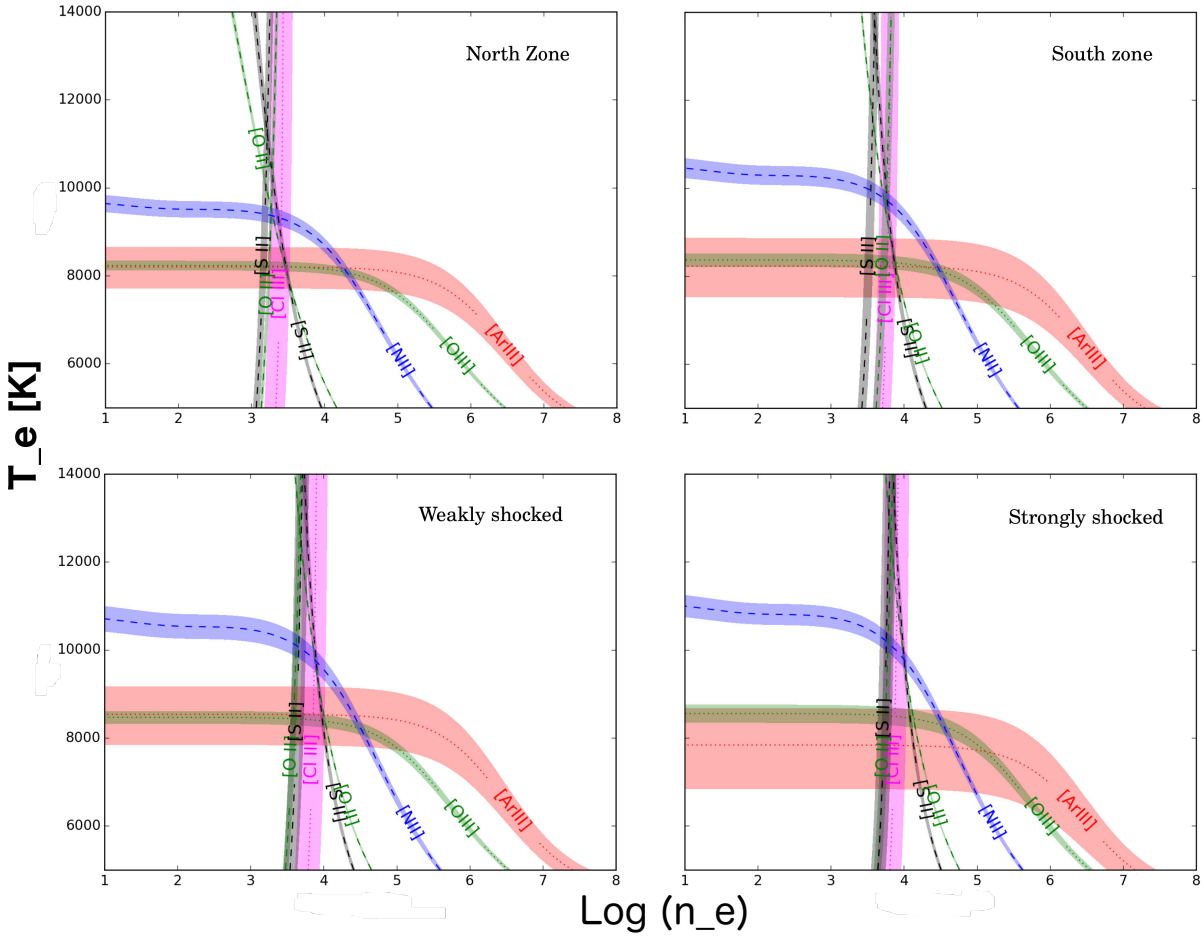

Figure 4.8: Temperature and density diagnostics for the four analyzed zones of the Orion Nebula.

We have followed the formalism developed by Peimbert (1967) to account for thermal inhomogeneities in the temperature structure of the nebula along the line of sight. This approach establishes an average temperature, T_0 and the mean square temperature inhomogeneities, t^2, defined as:

$$T_0(\text{ion}) = \frac{\int T_e(\mathbf{r}) n_e(\mathbf{r}) n_{\text{ion}}(\mathbf{r}) dV}{\int n_e(\mathbf{r}) n_{\text{ion}}(\mathbf{r}) dV}, \tag{4.6}$$

$$t^2(\text{ion}) = \frac{\int (T_e - T_0)^2 n_e(\mathbf{r}) n_{\text{ion}}(\mathbf{r}) dV}{T_0^2 \int n_e(\mathbf{r}) n_{\text{ion}}(\mathbf{r}) dV} \tag{4.7}$$

For the case of O^{2+} we can derive the following equation (Peimbert et al., 2004):

$$T_{4363/5007} = T_0 \left[(1 + \frac{t^2}{2} \left(\frac{91300\text{K}}{T_0} - 3 \right) \right]. \tag{4.8}$$

A similar equation can be derived for the T_0 of the low-ionization species.

Once T_0 and t^2 have been determined, Equation 4.8 is implemented to calculate the O^{2+} abundance (Peimbert & Costero, 1969; Esteban et al., 2004).

Table 4.3: LIST OF EMISSION LINE INTENSITIES FOR HH202-S AND THE ORION NEBULA[a].

			North zone		WS zone		SS zone		South zone	
λ	Ion	$f(\lambda)$	I	%err	I	%err	I	%err	I	%err
3587	He I	0.214	0.133	13	0.217	15	0.118	26	0.160	18
3614	He I	0.209	0.261	9	···	···	0.377	15	0.259	14
3634	He I	0.206	0.255	9	0.262	13	···	···	0.282	13
3676	H 22	0.199	0.448	7	···	···	···	···	···	···
3679	H 21	0.198	0.530	6	0.517	9	0.491	13	0.479	10
3683	H 20	0.198	0.556	6	0.530	9	0.564	12	0.520	10
3687	H 19	0.197	0.662	6	0.621	9	0.666	11	0.616	9
3692	H 18	0.196	0.815	5	0.751	8	0.805	10	0.763	8
3697	H 17	0.195	0.948	5	0.901	7	0.886	10	0.900	7
3704	H 16	0.194	1.539	4	1.518	6	1.522	7	1.524	6
3712	H 15	0.192	1.402	4	1.363	6	1.413	8	1.370	6
3722	H 14 + [S II]	0.190	0.628	6	1.619	5	1.823	7	1.470	6
3726	[O II]	0.190	85.732	1	60.557	1	66.532	1	63.628	1
3729	[O II]	0.189	52.546	1	29.413	2	29.748	2	28.685	2
3734	H 13	0.189	2.348	3	2.119	5	2.092	7	2.229	5
3750	H 12	0.186	3.086	3	3.118	4	3.093	6	3.070	4
3770	H 11	0.182	3.952	3	3.958	4	3.923	5	3.917	4
3798	H 10	0.177	5.218	2	5.236	3	5.188	4	5.156	3
3820	He I	0.174	1.066	5	1.097	7	1.073	9	1.095	7
3836	H 9	0.171	7.329	2	7.208	3	7.303	4	7.272	3
3856	Si II	0.167	···	···	0.283	13	0.297	16	0.185	16
3863	Si II	0.166	···	···	···		0.175	21	···	···
3869	[Ne III]	0.165	9.656	2	10.583	2	8.960	3	13.841	2
3889	H 8 + He I	0.162	17.338	1	15.693	2	15.250	3	16.300	2
3919	C II?	0.156	0.115	13	0.162	17	0.186	20	0.146	18
3927	He I	0.155	0.096	15	0.122	19	0.107	27	0.086	24
3933	O I	0.154	···	···	0.099	21	0.249	18	···	···

Table 4.3: continued.

			North zone		WS zone		SS zone		South zone	
λ	Ion	$f(\lambda)$	$I(\lambda)$	%err	$I(\lambda)$	%err	$I(\lambda)$	%err	$I(\lambda)$	%err
3970	[Ne III] + H 7	0.148	20.435	1	20.452	2	19.940	2	21.698	2
4009	He I	0.141	0.288	10	0.492	11	0.661	12	0.288	16
4026	He I	0.138	1.974	3	2.119	5	2.038	6	2.091	5
4069	[S II]	0.130	1.255	4	2.454	4	4.200	4	1.642	5
4076	[S II]	0.129	0.445	7	0.928	7	1.548	7	0.608	9
4102	Hδ	0.125	26.277	1	26.249	2	25.970	2	26.779	2
4114	[Fe II]	0.122	...	...	...		0.119	25	...	...
4121	He I	0.121	0.180	11	0.226	14	0.220	19	0.209	15
4131	O II	0.119	...	...	...		...	...	0.037	36
4144	He I	0.117	0.238	9	0.259	13	0.256	17	0.269	13
4155	O II + N II	0.116	...	...	...	...	0.058	36	0.051	30
4169	O II	0.113	0.039	22	...	...	0.027	53	0.043	33
4178	[Fe II]	0.112	...	...	...	...	0.076	31	...	...
4244	[Fe II]	0.100	0.327	8	0.133	18	0.432	13	...	...
4249	[Fe II]	0.099	...	...	0.232	14	0.223	18	0.183	16
4267	C II	0.096	0.234	9	0.209	14	0.213	19	0.216	15
4277	[Fe II]	0.095	0.045	21	0.064	26	0.215	19	0.041	34
4287	[Fe II]	0.093	0.112	13	0.108	20	0.449	13	0.082	24
4320	[Fe II]	0.088	...	...	...	...	0.153	22	...	...
4326	[Ni II]	0.086	...	...	0.123	18	0.274	16	0.053	29
4340	Hγ	0.084	46.866	1	47.007	1	46.735	2	46.622	1
4353	[Fe II]	0.082	...	...	...	...	0.119	25	...	...
4363	[O III]	0.080	0.829	5	1.033	6	0.903	9	1.060	7
4388	He I	0.076	0.515	7	0.613	9	0.583	12	0.586	9
4415	O II	0.072	0.146	11	0.235	13	0.607	11	0.129	19
4438	He I	0.068	0.051	19	0.059	26	0.050	38	0.065	26
4452	[Fe II]	0.065	...	...	0.058	27	0.157	21	0.032	37
4458	[Fe II]	0.062	...	...	0.050	29	0.136	23	...	...
4471	He I	0.055	4.350	2	4.708	3	4.494	4	4.594	3
4515	Fe II	0.046	...	...	...	...	0.040	42	...	...
4571	Mg I]	0.044	...	...	...	...	0.233	17	...	...
4581	[Cr III]	0.042	...	...	...	...	0.037	44	...	...
4595	[Co IV] ?	0.042	...	...	0.060	26	0.090	28	0.018	49
4607	[Fe III]	0.040	0.049	19	0.308	11	0.597	11	0.051	29
4630	N II	0.036	0.027	26	0.029	38	0.031	48	0.033	36
4642	O II	0.035	0.109	13	0.132	17	0.162	21	0.145	17
4650	O II	0.033	0.102	13	0.143	17	0.134	23	0.137	18
4658	[Fe III]	0.032	0.793	5	4.896	3	9.533	3	0.711	8

Table 4.3: continued.

			North zone		WS zone		SS zone		South zone	
λ	Ion	$f(\lambda)$	$I(\lambda)$	%err	$I(\lambda)$	%err	$I(\lambda)$	%err	$I(\lambda)$	%err
4665	[Fe III]	0.031	···	···	0.198	14	0.444	13	0.018	49
4701	[Fe III]	0.025	0.219	9	1.716	5	3.311	5	0.220	14
4711	[Ar IV]+He I	0.023	0.531	6	0.570	8	0.546	11	0.645	8
4728	[Fe II]	0.021	···	···	···	···	0.103	26	···	···
4734	[Fe III]	0.020	0.072	16	0.781	7	1.502	7	0.080	23
4740	[Ar IV]	0.019	0.021	29	···	···	···	···	···	···
4755	[Fe III]	0.017	0.142	11	0.937	7	1.753	6	0.140	17
4770	[Fe III]	0.014	0.070	16	0.600	8	1.165	8	0.071	25
4779	[Fe III]	0.013	0.044	20	0.383	10	0.808	9	0.043	31
4797	Cl I	0.010	0.049	19	···	···	0.069	32	···	···
4815	[Fe II]	0.007	0.065	17	0.104	19	0.328	15	0.047	30
4861	Hβ	0.000	98.818	1	100.004	1	99.705	1	98.332	1
4874	[Fe II]	0.000	···	···	···	···	0.108	25	···	···
4881	[Fe III]	-0.001	0.276	8	2.625	4	5.003	4	0.292	12
4890	[Fe II]	-0.001	0.033	23	0.070	24	0.229	17	0.022	43
4905	[Fe II]	-0.001	0.021	29	0.078	22	0.145	22	0.029	38
4922	He I	-0.002	1.205	4	1.325	6	1.307	8	1.272	6
4931	[Fe III]	-0.002	0.065	16	0.262	12	0.523	11	0.053	28
4959	[O III]	-0.004	85.528	1	96.013	1	79.275	1	101.927	1
4987	[Fe III]	-0.006	0.091	14	0.448	9	0.916	9	0.050	29
5007	[O III]	-0.007	253.745	1	283.142	1	238.115	1	304.533	1
5016	He I	-0.008	2.360	3	2.501	4	2.347	6	2.456	4
5041	Si II	-0.010	0.104	13	0.143	16	···	···	0.064	26
5048	He I	-0.010	0.240	10	0.253	16	0.240	22	0.250	16
5056	Si II	-0.011	0.181	10	0.236	13	0.253	16	0.139	17
5085	[Fe III]	-0.014	···	···	···	···	0.288	15	···	···
5112	[Fe II]	-0.017	0.031	24	0.028	37	0.157	21	···	···
5147	O II	-0.020	0.044	20	0.039	31	···	···	0.034	35
5159	[Fe II]	-0.022	0.097	13	0.280	12	1.000	8	0.067	25
5192	[Ar III]	-0.026	0.046	19	0.062	25	0.042	40	0.056	27
5198	[N I]	-0.027	0.518	6	0.218	13	0.230	17	0.293	12
5220	[Fe II]	-0.029	···	···	0.029	36	0.096	26	···	···
5262	[Fe II]	-0.035	0.085	14	0.120	18	0.457	12	0.046	30
5270	[Fe III]	-0.036	0.409	7	2.918	4	5.721	4	0.387	10
5299	O I	-0.040	0.039	21	···	···	0.070	31	0.027	39
5334	[Fe II]	-0.045	···	···	0.067	24	0.243	16	0.018	48
5376	[Fe II]	-0.052	···	···	0.029	36	0.164	15	···	···
5412	[Fe III]	-0.058	0.018	30	0.276	12	0.583	8	0.018	33

Table 4.3: continued.

			North zone		WS zone		SS zone		South zone	
λ	Ion	$f(\lambda)$	$I(\lambda)$	%err	$I(\lambda)$	%err	$I(\lambda)$	%err	$I(\lambda)$	%err
5433	[Fe II]	-0.061	···	···	···	···	0.077	21	0.017	35
5455	[Cr III]	-0.064	···	···	···	···	0.067	23	0.009	46
5472	[Cr III]	-0.067	···	···	···	···	0.090	20	···	···
5485	[Cr III]	-0.069	···	···	···	···	0.050	27	···	···
5496	[Fe II]	-0.071	···	···	···	···	0.036	31	···	···
5507	[Cr III]	-0.073	···	···	···	···	0.137	16	···	···
5513	O I	-0.075	0.032	23	···	···	···	···	0.022	30
5518	[Cl III]	-0.075	0.466	6	0.376	10	0.375	10	0.416	7
5527	[Fe II]	-0.077	···	···	0.061	25	0.267	11	0.015	37
5538	[Cl III]	-0.079	0.468	6	0.527	8	0.534	8	0.547	6
5552	[Cr III]	-0.081	···	···	0.115	18	0.260	12	···	···
5555	O I	-0.082	0.041	20	···	···	···		0.029	26
5667	N II	-0.103	0.021	28	···	···	0.037	30	0.028	27
5680	N II	-0.105	···	···	···	···	0.036	31	0.034	24
5715	[Cr III]	-0.106	···	···	···	···	0.124	17	···	···
5747	[Fe II]	-0.111	···	···	···	···	0.048	26	···	···
5755	[N II]	-0.120	0.735	5	0.965	6	1.302	5	0.790	5
5867	O I	-0.130	···	···	···	···	···	···	0.037	23
5876	He I	-0.144	12.920	1	13.351	2	13.535	2	13.614	2
5932	N II	-0.155	···	···	···	···	···	···	0.018	33
5942	N II	-0.157	···	···	···	···	···	···	0.026	27
5958	Si II + O I	-0.160	···	···	···	···	0.153	15	0.076	16
5979	Si II	-0.165	···	···	···	···	0.220	12	0.086	15
6000	[Ni III]	-0.169	···	···	···	···	0.122	16	0.013	38
6046	O I	-0.179	···	···	···	···	0.077	20	0.077	15
6312	[S III]	-0.234	1.560	3	1.966	4	1.935	4	1.760	3
6347	Si II	-0.242	···	···	0.251	11	0.300	10	0.132	12
6371	Si II	-0.247	···	···	0.129	16	0.146	14	0.067	16
6400	[Ni III]	-0.253	···	···	0.055	24	0.083	19	0.014	35
6440	[Fe II]	-0.261	···	···	···	···	0.052	24	···	···
6534	[Ni III]	-0.281	···	···	···	···	0.178	13	···	···
6548	[N II]	-0.284	18.984	1	18.795	2	23.987	1	16.555	1
6563	Hα	-0.287	288.294	1	289.239	1	288.392	1	288.675	1
6578	C II	-0.290	0.337	7	···	···	···	···	0.281	8
6583	[N II]	-0.291	56.261	1	57.606	1	72.984	1	49.607	1
6669	[Ni II]	-0.308	···	···	···	···	0.101	17	0.020	29
6678	He I	-0.310	3.375	2	3.658	3	3.516	3	3.590	2
6716	[S II]	-0.318	5.154	2	3.347	3	4.480	3	2.918	3

Table 4.3: continued.

			North zone		WS zone		SS zone		South zone	
λ	Ion	$f(\lambda)$	$I(\lambda)$	%err	$I(\lambda)$	%err	$I(\lambda)$	%err	$I(\lambda)$	%err
6731	[S II]	-0.321	7.142	2	6.040	2	8.430	2	4.990	2
6797	[Ni III]	-0.334	···	···	···	···	0.022	36	···	···
6946	[Ni III]	-0.364	···	···	0.029	32	···	···	···	···
7002	O I	-0.375	0.100	11	···	···	0.077	19	0.063	16
7065	He I	-0.388	4.297	2	4.802	3	4.582	3	5.536	2
7136	[Ar III]	-0.401	11.611	1	13.700	2	12.382	2	13.967	1
7155	[Fe II]	-0.405	0.059	15	0.304	10	1.436	4	0.050	17
7161	He I	-0.410	···	···	···	···	···	···	0.018	29
7231	C II	-0.419	0.063	14	0.093	17	0.078	18	0.078	14
7236	C II	-0.421	0.157	9	0.134	14	0.097	16	0.148	10
7254	O I	-0.424	···	···	···	···	0.111	15	0.081	14
7281	He I	-0.429	0.554	5	0.636	7	0.607	7	0.621	5
7291	[Ca II]	-0.431	···	···	0.138	14	0.572	7	···	···
7298	He I	-0.432	0.032	20	···	···	···	···	0.035	21
7320	[O II]	-0.436	3.673	2	6.784	2	9.330	2	5.244	2
7330	[O II]	-0.438	2.977	2	5.694	2	7.656	2	4.305	2
7341	Ca I	-0.440	···	···	···	···	···	···	0.042	19
7370	Ca I	-.445	···	···	···	···	···	···	0.025	24
7378	[Ni II]	-0.447	0.080	12	···	···	1.297	5	0.067	15
7388	[Fe II]	-0.449	···	···	0.079	18	0.285	10	···	···
7402	Ca II	-0.450	···	···	···	···	···	···	0.018	29
7412	[Ni II]	-0.453	···	···	···	···	0.137	14	0.019	28
7424	Ca I	-0.456	···	···	···	···	···	···	0.007	47
7443	S I	-0.459	···	···	···	···	···	···	0.017	29
7453	[Fe II]	-0.460	···	···	0.091	17	0.442	8	0.015	32
	$I(\mathrm{H}\beta)$[b]		8.96E-012		1.55E-012		1.49E-012		1.80E-011	
	$C(\mathrm{H}\beta)$		0.35		0.36		0.37		0.35	
	$\mathrm{EW_{abs}}(\mathrm{H}\beta)$		3.8		6.6		7.0		4.4	

[a]Emission lines corrected for reddening, underlying absorption and normalized with respect to the entire Balmer decrement.
[b]Dereddened flux for Hβ in units of erg cm^{-2} s^{-1}. The North and South zones are the sum of four 50-pixel long spectra from the Orion Nebula. The weakly and strongly shocked zones are the sum of four and three 3-pixel long spectra covering HH202-S (see text).

North Zone	South Zone	WS Zone	SS Zone
0.014 ± 0.005	0.022 ± 0.004	0.024 ± 0.006	0.039 ± 0.006

Table 4.4: t^2 values

4.2.2 Chemical composition

Ionic abundances were derived for O^+, O^{2+}, N^+, Ne^{2+}, S^+, S^{2+}, Cl^{2+}, Ar^{2+}, Fe^+, Fe^{2+}, and Ni^{2+}, from CELs using PyNeb. We also obtained He^+ from recombination lines and, just like in the previous section, the O^{2+} abundance was computed using the recombination lines of multiplet 1. The Fe^+ abundance was estimated using only [Fe II] λ7155 as it is the only line available in our observed range not affected by fluorescence; meanwhile, the Fe^{2+} abundance was determined using the emission of [Fe III] λ4734, λ4755 and λ4881, since these lines are the only ones that we can ensure that are not contaminated by emission of other ions given the spectral resolution of FORS 1.

The uncertainty associated to the ionic abundances was derived by direct propagation of uncertainties, from Equations 2.12 and 2.14 (see Appendix A). The uncertainties in emissivity were estimated from the percentage error of emission lines. For the case where $t^2 \neq 0.00$ the uncertainties associated were calculated through Equation 2.32, using the corresponding ΔE, $\Delta E'$ and temperature diagnostic for each ion.

The He^+ abundance was calculated from recombination lines using HELIO13, a software described in Peimbert et al. (2012), it uses a maximum likelihood method to perform a simultaneous fitting of n_e, τ_{3889}, the He^+ abundance, t^2, and T_0. We present the final adopted value of t^2 for each region in Table 4.4. In Table 4.6, we present the ionic abundances assuming both homogeneous and inhomogeneous temperature distributions: as mentioned in section 3 we prefer abundance determinations with $t^2 \neq 0.00$ because the shocked region obviously has inhomogeneous temperature, also CEL O^{2+} abundances agree better with the RL O^{2+} abundances when $t^2 \neq 0.00$ is used.

In order to calculate total abundances, we have to consider the contribution from unseen ions; this is done assuming a series of ionization correction factors (ICFs) from different sources. We don't expect this to be the case of oxygen, whose total abundance is simply the sum of O^+ and O^{2+}; any contribution from O^{3+} should be negligible because He II lines are

Diagnostic		North Zone	South Zone	WS Zone	SS Zone
T_e (K)	[O III]	8210 ± 120	8320 ± 170	8410 ± 160	8490 ± 220
	[Ar III]	8200 ± 440	8220 ± 650	8530 ± 670	7830 ± 890
	[N II]	9370 ± 200	9800 ± 300	10060 ± 300	10125 ± 240
	Adopted HI	8210 ± 150	8320 ± 200	8410 ± 200	8490 ± 300
	Adopted LI	9500 ± 250	9780 ± 300	10230 ± 300	10260 ± 350
n_e (cm^{-3})	[Cl III]	2500 ± 1100	5980^{+2700}_{-1900}	7200^{+5100}_{-3000}	7550^{+5300}_{3000}
	[O II]	1860 ± 110	5720 ± 800	4230 ± 500	6300 ± 900
	[S II]	1530 ± 200	3500 ± 600	4590 ± 1100	5800 ± 1500
	Adopted HI	2500 ± 1000	5980 ± 2000	7200 ± 3000	7550 ± 3000
	Adopted LI	1800 ± 200	4750 ± 500	4250 ± 600	6100 ± 900

Table 4.5: Physical conditions from combined spectra

absent from our spectra —O^{2+} and He^+ have a similar ionization energy $\sim$ 54 eV—.

For nitrogen we have used the classic ICF, to account for the presence of N^{2+}:

$$\frac{N}{H} = \left[\frac{O^+ + O^{2+}}{O^+}\right]_{CEL} \times \frac{N^+}{H^+} = ICF(N^{2+}) \times \frac{N^+}{H^+}. \tag{4.9}$$

The total neon abundance has a contribution from Ne^{2+}, which we have taken in consideration using the ICF from Peimbert & Costero (1969):

$$\frac{Ne}{H} = \left[\frac{O^+ + O^{2+}}{O^{2+}}\right]_{CEL} \times \frac{Ne^{2+}}{H^+} = ICF(Ne^{2+}) \times \frac{Ne^{2+}}{H^+}. \tag{4.10}$$

Besides S^+ and S^{2+}, it is known that S^{3+} must be present in H II regions from the work of Stasińska (1978):

$$\frac{S}{H} = \left[1 - \left[\frac{O^+}{O^+ + O^{2+}}\right]^3_{CEL}\right]^{-1/3} \times \frac{S^+ + S^{2+}}{H^+} = ICF(S^+ + S^{2+}) \times \frac{S^+ + S^{2+}}{H^+}. \tag{4.11}$$

Helium has to be corrected for the presence He^0, we have done this using the ICF derived by Peimbert et al. (1992):

$$\frac{He}{H} = \left[1 + \frac{S^+}{S - S^+}\right] \times \frac{He^+}{H^+} = ICF(He^+) \times \frac{He^+}{H^+}, \tag{4.12}$$

however, as Delgado-Inglada et al. (2014) point out, this result has to be taken with reservation, since the population of helium ions depends on the effective temperature of the ionizing stars, and that of sulfur on the ionization parameter.

We have observed [Cl III] emission lines in our spectra, however Cl^{+} and possibly Cl^{3+} also contribute to the total chlorine abundance. Delgado-Inglada et al. (2014) propose an ICF which, although intended for use in planetary nebulae, can be used in this case as it depends on the ionic fraction of oxygen and the observed abundance of Cl^{2+}:

$$\begin{aligned}\frac{\mathrm{Cl}}{\mathrm{H}} &= \left(4.1620 - 4.1622\left[\frac{\mathrm{O}^{2+}}{\mathrm{O}^{+}+\mathrm{O}^{2+}}\right]^{0.21}\right)^{0.75} \times \frac{\mathrm{Cl}^{2+}}{\mathrm{O}^{+}} \times \frac{\mathrm{O}^{+}+\mathrm{O}^{2+}}{\mathrm{H}^{+}} \\ &= \mathrm{ICF}\left(\frac{\mathrm{Cl}^{2+}}{\mathrm{O}^{+}}\right) \times \frac{\mathrm{Cl}^{2+}}{\mathrm{O}^{+}} \times \frac{\mathrm{O}^{+}+\mathrm{O}^{2+}}{\mathrm{H}^{+}}; \end{aligned} \tag{4.13}$$

this is valid when the ionic fraction of O^{2+} —the term in brackets— takes a value between 0.02 and 0.95.

It is known that Ar^{+} can contribute a significant fraction to the total abundance. For this work, we have employed the ICF obtained by Delgado-Inglada et al. (2014) computed from Cloudy photoionization models, which depends only on Ar^{2+} lines:

$$\frac{\mathrm{Ar}}{\mathrm{H}} = 10^{\left(\frac{0.3\omega}{0.4-0.3\omega}-0.05\right)} \times \frac{\mathrm{Ar}^{2+}}{\mathrm{H}^{+}} = \mathrm{ICF}(\mathrm{Ar}^{2+}) \times \frac{\mathrm{Ar}^{2+}}{\mathrm{H}^{+}}$$

with $\omega = \mathrm{O}^{2+}/(\mathrm{O}^{+}+\mathrm{O}^{2+})$.

Uncertainties in atomic data affect some ions more than others; given the complex structure of Fe^{+} and Fe^{2+}, the atomic data currently available does not yet represent a complete picture of this element; furthermore is known that many [Fe II] lines are affected by fluorescence. For computing the total iron abundance, Rodríguez & Rubin (2005) propose two ICFs based on observations and photoionization models which require only [Fe III] lines. We have decided to use their observational ICF since the one from the models produces results for total iron abundance that would imply a complete destruction of Fe from interstellar dust grains (see section 4.3.1), something that is not expected in these observations since we have substantial amounts of unshocked gas in front and behind the shocked region; also this shock is not fast enough to be expected to destroy all the dust grains it encounters. Thus

$$\frac{\mathrm{Fe}}{\mathrm{H}} = 1.1\left(\frac{\mathrm{O}^{+}}{\mathrm{O}^{++}}\right)^{0.58} \times \frac{\mathrm{Fe}^{++}}{\mathrm{O}^{+}} \times \frac{\mathrm{O}}{\mathrm{H}}. \tag{4.14}$$

Nickel poses similar problems to iron in the sense that [Ni II] lines may be affected by fluorescence. Until recently, most studies have used an ICF for Nickel that is based on the similarity between the ionization potentials of Fe^+ and Ni^+. Based on a large grid of photoionization models, Delgado-Inglada et al. (2016) have derived two ICFs for Ni that require only [Ni III] lines, applicable for both H II regions and planetary nebulae. From Equation 6 of their paper —applicable when He^{2+} is not present— we have that

$$\frac{\mathrm{Ni}}{\mathrm{H}} = \left(1.1 - 0.9\frac{\mathrm{O}^{2+}}{\mathrm{O}^{+}+\mathrm{O}^{2+}}\right) \times \frac{\mathrm{Ni}^{2+}}{\mathrm{O}^{+}} \times \left(\frac{\mathrm{O}^{+}+\mathrm{O}^{2+}}{\mathrm{H}^{+}}\right) \tag{4.15}$$

$$= \mathrm{ICF}\left(\frac{\mathrm{Ni}^{2+}}{\mathrm{O}^{+}}\right) \times \frac{\mathrm{Ni}^{2+}}{\mathrm{O}^{+}} \times \left(\frac{\mathrm{O}^{+}+\mathrm{O}^{2+}}{\mathrm{H}^{+}}\right). \tag{4.16}$$

We have used [Ni III] $\lambda\lambda$ 4326, 6000, and 6401 to calculate the total Ni^{2+} abundance, as these lines are not contaminated by others in our spectra.

Total abundances are presented in Table 4.7 considering a both homogeneous ($t^2 = 0.00$) and inhomogeneous temperature ($t^2 \neq 0.00$). The uncertainties associated to O/H, N/H, Ne/H, Fe/H and S/H were obtained through direct propagation of uncertainties (see Appendix A), incorporating the uncertainty associated to the corresponding ICF; when we have referred to the ICFs by Delgado-Inglada et al. (2014) we have estimated the error following the methodology indicated in that paper.

Ion	North zone		South zone		WS zone		SS zone	
	$t^2 = 0.00$	$t^2 = 0.014$	$t^2 = 0.00$	$t^2 = 0.022$	$t^2 = 0.00$	$t^2 = 0.024$	$t^2 = 0.00$	$t^2 = 0.039$
Ar^{2+}	6.25 ± 0.02	6.34 ± 0.03	6.31 ± 0.03	6.45 ± 0.03	6.30 ± 0.03	6.44 ± 0.04	6.23 ± 0.04	6.48 ± 0.04
Cl^{2+}	5.08 ± 0.04	5.19 ± 0.05	5.11 ± 0.03	5.27 ± 0.06	5.08 ± 0.03	5.25 ± 0.06	5.06 ± 0.03	5.35 ± 0.07
Fe^{+}	4.72:	4.77:	4.59:	4.66:	5.34:	5.41:	6.00:	6.12:
Fe^{2+}	5.60 ± 0.04	5.65 ± 0.05	5.52 ± 0.06	5.60 ± 0.06	6.38 ± 0.03	6.46 ± 0.03	6.64 ± 0.04	6.77 ± 0.05
N^{+}	7.13 ± 0.03	7.18 ± 0.03	7.05 ± 0.03	7.12 ± 0.04	7.05 ± 0.03	7.12 ± 0.03	7.17 ± 0.04	7.29 ± 0.04
Ne^{2+}	7.42 ± 0.03	7.54 ± 0.05	7.55 ± 0.04	7.73 ± 0.06	7.41 ± 0.05	7.61 ± 0.05	7.31 ± 0.06	7.63 ± 0.07
Ni^{2+}	···	···	4.46 ± 0.10	4.60 ± 0.11	4.99 ± 0.07	5.13 ± 0.07	5.24 ± 0.06	5.43 ± 0.07
O^{+}	7.91 ± 0.02	7.97 ± 0.04	7.80 ± 0.03	7.90 ± 0.04	7.69 ± 0.02	7.79 ± 0.03	7.79 ± 0.03	7.95 ± 0.05
O^{2+}	8.29 ± 0.02	8.38 ± 0.03	8.34 ± 0.04	8.49 ± 0.05	8.30 ± 0.03	8.47 ± 0.04	8.20 ± 0.04	8.50 ± 0.05
O^{2+}_{RL}	8.38 ± 0.04		8.49 ± 0.05		8.47 ± 0.05		8.51 ± 0.06	
S^{+}	5.70 ± 0.02	5.75 ± 0.03	5.63 ± 0.04	5.70 ± 0.06	5.62 ± 0.02	5.69 ± 0.03	5.84 ± 0.02	5.95 ± 0.05
S^{2+}	6.94 ± 0.05	7.06 ± 0.06	6.96 ± 0.06	7.14 ± 0.07	6.98 ± 0.06	7.18 ± 0.07	6.95 ± 0.07	7.27 ± 0.09
He^{+}_{RL}	10.926 ± 0.004	10.922 ± 0.004	10.952 ± 0.006	10.936 ± 0.005	10.951 ± 0.006	10.940 ± 0.006	10.959 ± 0.007	10.922 ± 0.008

Table 4.6: Ionic abundances

Element	North zone		South zone		WS zone		SS zone	
	$t^2 = 0.00$	$t^2 = 0.014$	$t^2 = 0.00$	$t^2 = 0.022$	$t^2 = 0.00$	$t^2 = 0.024$	$t^2 = 0.00$	$t^2 = 0.039$
Ar	$6.31\pm^{0.2}_{0.52}$	$6.41\pm^{0.2}_{0.52}$	$6.40\ \pm^{0.2}_{0.52}$	$6.55\pm^{0.2}_{0.52}$	$6.40\ \pm^{0.2}_{0.52}$	$6.56\pm^{0.2}_{0.52}$	$6.28\pm^{0.2}_{0.52}$	$6.58\pm^{0.2}_{0.52}$
Cl	$5.22\ \pm^{0.06}_{0.14}$	$5.32\pm^{0.06}_{0.14}$	$5.26\ \pm^{0.06}_{0.14}$	$5.42\pm^{0.06}_{0.14}$	$5.24\ \pm^{0.06}_{0.14}$	$5.42\ \pm^{0.06}_{0.14}$	$5.19\pm^{0.06}_{0.14}$	$5.50\ \pm^{0.06}_{0.14}$
Fe	5.95 ± 0.04	6.00 ± 0.06	5.91 ± 0.06	5.99 ± 0.08	6.78 ± 0.05	6.87 ± 0.05	7.00 ± 0.06	7.15 ± 0.07
N	7.67 ± 0.03	7.73 ± 0.05	7.71 ± 0.02	7.81 ± 0.06	7.76 ± 0.03	7.88 ± 0.05	7.71 ± 0.02	7.95 ± 0.06
Ne	7.57 ± 0.03	7.69 ± 0.04	7.66 ± 0.05	7.83 ± 0.06	7.51 ± 0.04	7.69 ± 0.05	7.45 ± 0.07	7.74 ± 0.08
Ni	···	···	4.72 ± 0.03	4.88 ± 0.04	5.28 ± 0.04	5.45 ± 0.03	5.45 ± 0.04	5.69 ± 0.04
O_{CEL}	8.44 ± 0.02	8.52 ± 0.02	8.45 ± 0.03	8.59 ± 0.04	8.39 ± 0.03	8.56 ± 0.03	8.34 ± 0.03	8.61 ± 0.04
O_{RL}	8.53 ± 0.04		8.60 ± 0.05		8.57 ± 0.05		8.65 ± 0.06	
S	6.98 ± 0.04	7.09 ± 0.05	6.98 ± 0.06	7.16 ± 0.07	7.00 ± 0.06	7.19 ± 0.07	7.00 ± 0.07	7.30 ± 0.08
He_{RL}	10.950 ± 0.005	10.94 ± 0.01	10.972 ± 0.007	10.96 ± 0.01	10.973 ± 0.007	10.96 ± 0.01	10.990 ± 0.009	10.95 ± 0.01

Table 4.7: Total abundances

4.3 Discussion

The results obtained here for T_e and n_e for the North and South zones agree with previous determinations by Esteban et al. (2004) and Rubin et al. (2003). For the shocked zones the only available reference is the work of Mesa-Delgado et al. (2009a); while our results for T_e are in considerable agreement for the unshocked zones, in the shocked windows we find differences of $\sim$ 300 K for high-ionization and $\sim$1000 K for low-ionization in our strongly shocked zone. The authors of that work also adopt a considerably higher density (17 430 $\pm$ 2360 cm^{-3}), and they use the same value as representative of both high and low ionization zones. These differences may be explained by the fact that, in our observations, we are analyzing a volume of gas which contains both shocked and unshocked components, since the spectral resolution of FORS 1 does not permit us to extract the purely shocked gas emission. Also, it must be noted that the Strongly Shocked Zone analyzed in this thesis does not necessarily correspond with the Shock Component studied in Mesa-Delgado et al. (2009a): whereas our SS Zone was defined from the maximum O/H ratio presented in Figure 4.7, the Shock Component studied in Mesa-Delgado et al. (2009a) was extracted directly for every emission line, made possible thanks to the spectral resolution of UVES. Figures 4.5 and 4.6 may support this fact since the windows with maximum T_e and n_e do not coincide with the Strongly Shocked Zone we defined.

Just as in our analysis from section 4, we have found that the ADF associated to O^{2+} and O is greater at the SS zone. This connection between Herbig-Haro objects and the ADF had been reported previously by Mesa-Delgado et al. (2008) who found several above-average increases in the ADF associated with Herbig-Haro objects 202, 203, and 204 in the Orion Nebula; however, the cause behind these high ADF values —being temperature fluctuations, or any other mechanism— remained uncertain. They concluded that thermal inhomogeneities, if they exist, should be lower than their spatial resolution limit of 1″. Eventually Mesa-Delgado et al. (2009a) found that the t^2 parameter increases significantly at the shock component of HH 202.

As we can see in Tables 4.6 and 4.7, O^{2+} and O abundances determined from CELs and RLs are irreconcilable at the Strongly Shocked Zone unless we consider the presence of temperature fluctuations. In their study of HH 202–S, Mesa-Delgado et al. (2009a) reported values of $t^2 = 0.049$ and $t^2 = 0.050$ at the center of the shock, which imply a greater

abundance for $O_{CEL} = 8.76 \pm 0.06$ that is not compatible with their estimate for $O_{RL} = 8.65 \pm 0.05$. As noted in their paper, this may indicate that the t^2 paradigm is not applicable in the case of the shocked volume of gas.

In this work we have determined that, at the Strongly Shocked zone, the mean squared temperature fluctuations show a peak value of $t^2 = 0.039 \pm 0.006$ which, as can be seen in Tables 4.6 and 4.7, reconciles the ionic O^{2+} abundance and the total oxygen abundance determined from CELs and RLs in all of the observed zones. This result and the behavior observed in Figure 4.7 appear to indicate that the t^2 parameter is intrinsically linked to shocks; suggesting that shocks embedded in the structure of the nebulae may be responsible for an important fraction of the observed t^2 parameter in H II regions, as well as in the observed ADF. However, as stated at the beginning of this section, the volume of gas we examined contains both shocked and unshocked components that we cannot separate, as a consequence, our reported t^2 value is not representative of the purely shocked gas and it is not possible to estimate in what amount it would be modified if we were to isolate the purely shocked component. Clearly, a similar analysis to the one performed here on other spatially resolved interstellar shocks would contribute to elaborate into the possible connection between shocks and the t^2 parameter.

4.3.1 Dust destruction

As Table 4.3 shows, emission lines of refractory elements such as Fe and Ni are much brighter in the weakly and stongly shocked zones. In this analysis we will use Fe to explore the extension of dust destruction since it is known that about 90% of it is depleted in dust grains (Rodríguez & Rubin, 2005; Peimbert & Peimbert, 2010).

The total abundance of iron depends on the ICF used to calculate it. Rodríguez & Rubin (2005) derived two ICFs based on observations and photoionization models. Several works (Esteban et al., 2004; Mesa-Delgado et al., 2009a; Delgado-Inglada et al., 2016) use the ICF from photoionization models. From our data we find an increase in 1.15 dex over the average iron abundance of the unshocked zones using the observational ICF which, taking the solar value ($\log(Fe/H) = 7.50 \pm 0.04$ from Asplund et al. (2009)) as reference, , implies that $50 \pm 10\%$ of the iron previously trapped in dust is released by the shock, on the other hand, the ICF derived from photoionization models delivers a value of 80% for the amount

of Fe released. The latter value would imply a nearly total dust destruction, which is only reached by the shock of an expanding supernova (Gall et al., 2014), and seems extreme for a Herbig-Haro object, especially if we take into account the fact that the area we are observing includes both shocked and unshocked material. Given these results, we favored the observational ICF by Rodríguez & Rubin (2005) and its implications.

It has been suggested (Podio et al., 2009) that some materials released by dust destruction such as Calcium can condense and be reincorporated into the dust phase. The amount of iron present in the Weakly Shocked Zone may be due to condensation, or it may be caused by a partial destruction of dust grains. The WS Zone is undoubtedly influenced by the shock, but the gas Fe/H and O/H content is not maximum. Unfortunately, we cannot ascertain that condensation, or partial destruction is responsible for the measured abundances. Firstly, it must be noted that the slit was not oriented parallel to the direction of the gas flow (O'Dell & Henney, 2008), but instead it was positioned with the intention of covering the brightest part of HH 202. Also, we must not forget that the WS Zone presents two components —shocked and unshocked gas— that we cannot separate.

In order to study the possible condensation of heavy elements into dust grains, it would be necessary to place the slit parallel to the gas flow and separate the purely shocked gas from the static component. Identifying the hypothetical 'condensation zone' would be a challenge too, since the SS and WS zones are quite small, covering 9 and 12 pixels respectively.

We can estimate the amount of nickel released by the shock as well. This element is not as abundant as iron, magnesium or silicon, and it is not expected to be mixed solely with oxygen in dust grains. Scott et al. (2015) have derived a value for $\mathrm{Ni}_{\odot} = 6.20 \pm 0.04$. From our determinations (using atomic data from Bautista (2001)), we find that 25 ± 10 % of Ni is released by the shockwave. This suggests that the shock is not as efficient in incorporating nickel to the gas phase as it is to iron. A deeper discussion on this subject can be found in Delgado-Inglada et al. (2016).

In H II regions, it is expected that iron and oxygen are found predominantly in compounds such as ferrous oxide (FeO), therefore we have assumed that dust O and Fe are destroyed in the same fraction. The iron to oxygen ratio can be used as an indicator of the degree of dust destruction by calculating its value in the center of HH 202-S and comparing it with the surrounding gas. Considering our average abundance for North and South zones

and the value at the Strongly Shocked zone we can extrapolate to a total destruction by taking the solar value of $\log(\mathrm{Fe/O})_{\odot} = -1.22$ (Grevesse et al., 2015; Asplund et al., 2009) as reference; with these considerations we find that the O depletion factor of the ambient gas to be -0.12 ± 0.04. This is represented in Figure 4.9, where the 'unshocked' point is the weighted average of the North Zone and South Zone values. With these assumptions, 57 ± 10 % of the dust is destroyed at the Strongly Shocked Zone.

There are two other methods that can be used to estimate the amount of depletion of oxygen. The first one consists in comparing the oxygen abundance in the ionized gas with the oxygen abundance in the stars of the Orion Nebula. The oxygen abundance from B-type stars of the Ori-OB1 association has been measured to be 8.74 ± 0.04 (Simón-Díaz & Stasińska, 2011). With this reference value and our $\mathrm{O_{RL}}$ determination we find a depletion factor of -0.18 ± 0.05 dex. Using the same method, Mesa-Delgado et al. (2009a) estimate a depletion factor of -0.17 ± 0.06.

The last method comes from the fact that dust grains are species formed from Mg, Si, Fe, and O such as olivine (Mg, Fe)$_2$SiO$_4$ and pyroxene (Mg, Fe)SiO$_3$. The depletion factor can be estimated then from the abundances of said elements in the gas. From these assumptions, the accepted value for the depletion factor in the Orion Nebula has been measured to be -0.10 ± 0.04. The results for the depletion factors obtained through different methods are summarized in Table 4.8.

First we must notice that our value for the depletion factor agrees excellently with those from the other two methods, thanks to the quality of our observations and data reduction. We have calculated the weighted average (see Appendix A) of the three methods using our results and those of Mesa-Delgado et al. (2009a) from the previous paragraphs obtaining a depletion factor of -0.126 ± 0.024.

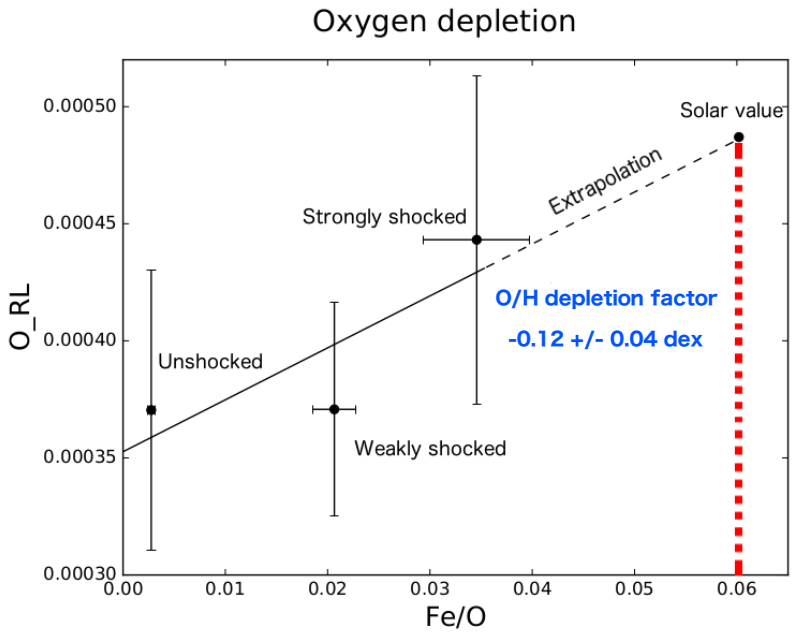

Figure 4.9: Oxygen abundance in gas. The leftmost point is an average of the nebular (unshocked) windows; the two others are from weakly and strongly shocked zones. The dashed line represents extrapolation to a total dust destruction.

Method	Value	Reference
Solar Fe/O ratio	-0.12 ± 0.04	This work
	$-0.11^{+0.11}_{-0.14}$	Mesa-Delgado et al. (2009a)
Comparison with Orion stars	-0.18 ± 0.05	This work
	-0.17 ± 0.06	Mesa-Delgado et al. (2009a)
Molecular composition	-0.10 ± 0.04	Esteban et al. (1998); Mesa-Delgado et al. (2009a)

Table 4.8: Oxygen depletion factors

Chapter 5

Conclusions

We have performed a long-slit spectroscopic analysis of Herbig-Haro 202 using the FORS 1 spectrograph of the VLT. We have determined the spatial variations in electron temperature and density across the Orion Nebula and compared them to the ones in the shock. We have shown that oxygen (O/H) abundances determined from collisionally excited lines and recombination lines are irreconcilable at the brightest part of the shock unless we consider the existence of thermal inhomogeneities along the line of sight, in agreement with a previous study by Mesa-Delgado et al. (2009a). The Abundance Discrepancy Factor associated to O^{2+} and O is greater at the strongly shocked zone, coinciding with the peak of the t^2 parameter; this fact suggests that interstellar shocks may contribute an important fraction to the t^2 parameter. Iron (Fe) abundance also shows a peak at this zone, an effect that we attribute to dust destruction by the gas flow, which releases iron into the gas phase.

The spatial analysis permitted us to hand pick the zones at which the Fe/H and O/H content was greatest, allowing us to estimate the amount of iron and oxygen atoms released due to the destruction of interstellar dust by the shock of HH 202.

Spectra from four different zones of the Orion Nebula were combined to increase the signal to noise ratio. We identified a total of 169 different emission lines, including 159 in the strongly shocked zone, that we used to derive physical conditions with high precision.

Chemical abundances for He, O, N, Ar, Cl, Ne, S, Fe and Ni were calculated assuming both homogeneous temperature and thermal inhomogeneities. We showed that O abundances from CELs and RLs can be made to agree by incorporating the t^2 parameter pro-

posed by Peimbert (1967) although, since the volume of gas we have studied contains both shocked and unshocked components, the question of wether the t^2 paradigm can be applied to the purely shocked gas remains open. Also, we have reproduced the results obtained by Mesa-Delgado et al. (2009a), complementing that work by providing a spatial analysis of the physical conditions and oxygen abundance across HH 202 and the surrounding gas.

Using Fe/O as an indicator, we have shown that dust destruction is taking place at the apex of HH 202, which amounts to 57 $\pm$ 10 %.

Comparing the abundance of Ni in the static gas with the Strongly Shocked zones we have found that 25 % of Ni is released from dust by the gas flow, suggesting that the shock is not as efficient in incorporating Ni to the ambient gas.

Comparing the total oxygen abundance at the Strongly Shocked Zone with the ambient gas, and taking the solar value as reference, we found the depletion factor of oxygen to be -0.12 ± 0.04 dex. We also compared the total oxygen abundance with respect to the abundance in the stars of the Orion Nebula, finding a depletion factor or -0.18 ± 0.05 dex

Finally, we averaged our results with those obtained by Mesa-Delgado et al. (2009a) using the same methods, obtaining a depletion factor for oxygen of -0.126 ± 0.024.

Appendix A

Propagation of uncertainties

If various quantities x, . . . , w are measured with small uncertainties δx, . . . , δw, and the measured values are used to calculate some quantity q, then the uncertainties in x, . . . , w cause an uncertainty in q given by the general equation

$$\delta q = \sqrt{(\frac{\partial q}{\partial x}\delta x)^2 + \cdots + (\frac{\partial q}{\partial z}\delta z)^2}. \tag{A.1}$$

Weighted Averages

If x_1, . . . , x_N are measurements of the same quantity x, with known uncertainties σ_1, . . . , σ_N, then the best estimate x is the weighted average

$$x_{\text{wav}} = \frac{\Sigma w_i x_i}{\Sigma w_i}, \tag{A.2}$$

where the weight $w_i = 1/\sigma_i^2$.

The uncertainty associated is

$$\sigma_{\text{wav}} = \frac{1}{\sqrt{\Sigma w_i}}. \tag{A.3}$$

Bibliography

Aggarwal, K. M., & Keenan, F. P. 1999, ApJS, 123, 311

Asplund, M., Grevesse, N., Sauval, A. J., & Scott, P. 2009, ARA&A, 47, 481

Bautista, M. A. 2001, A&A, 365, 268

Blagrave, K. P. M., Martin, P. G., & Baldwin, J. A. 2006, ApJ, 644, 1006

Butler, K., & Zeippen, C. J. 1989, A&A, 208, 337

Canto, J., Goudis, C., Johnson, P. G., & Meaburn, J. 1980, A&A, 85, 128

Cardelli, J. A., Clayton, G. C., & Mathis, J. S. 1989, ApJ, 345, 245

Costero, R., & Peimbert, M. 1970, Boletin de los Observatorios Tonantzintla y Tacubaya, 5, 229

Chaffee, F. H., Jr., & Schroeder, D. J. 1976, ARA&A, 14, 23

Delgado-Inglada, G., Mesa-Delgado, A., García-Rojas, J., Rodríguez, M., & Esteban, C. 2016, MNRAS, 456, 3855

Delgado-Inglada, G., Morisset, C., & Stasińska, G. 2014, MNRAS, 440, 536

Draine, B. T. 2011, Physics of the Interstellar and Intergalactic Medium by Bruce T. Draine. Princeton University Press, 2011. ISBN: 978-0-691-12214-4,

Escalante, V., Morisset, C., & Georgiev, L. 2012, MNRAS, 426, 2318

Esteban, C., Peimbert, M., García-Rojas, J., et al. 2004, MNRAS, 355, 229

Esteban, C., Peimbert, M., Torres-Peimbert, S., & Escalante, V. 1998, MNRAS, 295, 401

Galavis, M. E., Mendoza, C., & Zeippen, C. J. 1995, A&AS, 111, 347

Galavis, M. E., Mendoza, C., & Zeippen, C. J. 1997, A&AS, 123

Gall, C., Hjorth, J., Watson, D., et al. 2014, Nature, 511, 326

García-Rojas, J. 2007, Ph.D. Thesis,

Grevesse, N., Scott, P., Asplund, M., & Sauval, A. J. 2015, A&A, 573, A27

Hamuy, M., Walker, A. R., Suntzeff, N. B., et al. 1992, PASP, 104, 533

Hamuy, M., Suntzeff, N. B., Heathcote, S. R., et al. 1994, PASP, 106, 566

Johansson, S., Zethson, T., Hartman, H., et al. 2000, A&A, 361, 977

Luridiana, V., Morisset, C., & Shaw, R. A. 2015, A&A, 573, A42

Mendoza, C., & Zeippen, C. J. 1982, MNRAS, 198, 127

Mendoza, C., & Zeippen, C. J. 1982, MNRAS, 199, 1025

Mendoza, C. 1983, Planetary Nebulae, 103, 143

Mesa-Delgado, A., Esteban, C., & García-Rojas, J. 2008, ApJ, 675, 389-404

Mesa-Delgado, A., Esteban, C., García-Rojas, J., et al. 2009a, MNRAS, 395, 855

Mesa-Delgado, A., López-Martín, L., Esteban, C., García-Rojas, J., & Luridiana, V. 2009b, MNRAS, 394, 693

Mouri, H., & Taniguchi, Y. 2000, ApJ, 534, L63

O'Dell, C. R., & Henney, W. J. 2008, AJ, 136, 1566

Osterbrock, D. E., Tran, H. D., & Veilleux, S. 1992, ApJ, 389, 305

Osterbrock, D. E., & Ferland, G. J. 2006, Astrophysics of gaseous nebulae and active galactic nuclei, 2nd. ed. by D.E. Osterbrock and G.J. Ferland. Sausalito, CA: University Science Books, 2006,

Peimbert, A., & Peimbert, M. 2010, ApJ, 724, 791

Peimbert, M. 1967, ApJ, 150, 825

Peimbert, M., & Costero, R. 1969, Boletin de los Observatorios Tonantzintla y Tacubaya, 5, 3

Peimbert, M., Torres-Peimbert, S., & Ruiz, M. T. 1992, , 24, 155

Peimbert, M., Storey, P. J., & Torres-Peimbert, S. 1993, ApJ, 414, 626

Peimbert, A., Peimbert, M., & Luridiana, V. 2002, ApJ, 565, 668

Peimbert, A., & Peimbert, M. 2010, ApJ, 724, 791

Peimbert, M., Peimbert, A., Ruiz, M. T., & Esteban, C. 2004, ApJS, 150, 431

Peimbert, A., & Peimbert, M. 2010, ApJ, 724, 791

Peimbert, A., Peña-Guerrero, M. A., & Peimbert, M. 2012, ApJ, 753, 39

Peimbert, A., Peimbert, M., & Luridiana, V. 2016, , 52, 419

Peña-Guerrero, M. A., Peimbert, A., Peimbert, M., & Ruiz, M. T. 2012, ApJ, 746, 115

Podio, L., Medves, S., Bacciotti, F., Eislöffel, J., & Ray, T. 2009, A&A, 506, 779

Pradhan, A. K., Montenegro, M., Nahar, S. N., & Eissner, W. 2006, MNRAS, 366, L6

Quinet, P. 1996, A&AS, 116, 573

Rodríguez, M., & Rubin, R. H. 2005, ApJ, 626, 900

Rubin, R. H., Martin, P. G., Dufour, R. J., et al. 2003, MNRAS, 340, 362

Scott, P., Asplund, M., Grevesse, N., Bergemann, M., & Sauval, A. J. 2015, A&A, 573, A26

Seaton, M. J. 1979, MNRAS, 187, 73P

Simón-Díaz, S., & Stasińska, G. 2011, A&A, 526, A48

Simpson, J. P., Colgan, S. W. J., Rubin, R. H., Erickson, E. F., & Haas, M. R. 1995, ApJ, 444, 721

Stasińska, G. 1978, A&A, 66, 257

Storey, P. J. 1994, A&A, 282, 999

Storey, P. J., & Hummer, D. G. 1995, MNRAS, 272, 41

Storey, P. J., & Zeippen, C. J. 2000, MNRAS, 312, 813

Tayal, S. S., & Gupta, G. P. 1999, ApJ, 526, 544

Tayal, S. S. 2007, ApJS, 171, 331

Tayal, S. S. 2011, ApJS, 195, 12

Tayal, S. S., & Zatsarinny, O. 2010, ApJS, 188, 32

Vilchez, J. M., & Esteban, C. 1996, MNRAS, 280, 720

Wiese, W. L., Fuhr, J. R., & Deters, T. M. 1996, Journal of Physical and Chemical Reference Data, Monograph 7. Melville, NY: AIP Press,

Zhang, H. 1996, A&AS, 119, 523